



## MASTERS THESIS

IMPERIAL COLLEGE LONDON

DEPARTMENT OF CHEMISTRY

---

# Ab Initio Modelling of a Gold Nanojunction

---

*Author:*  
Jad Jaafar

*Supervisor I:*  
Dr. Clotilde Cucinotta

*Supervisor II:*  
Prof. Nicholas Harrison

August 25, 2022

## Acknowledgements

Foremost, I would like to express deep gratitude towards my esteemed supervisors Dr. Clotilde Cucinotta and Prof. Nicholas Harrison for their continuous support, advice and patience. Thanks to their wisdom and assistance, I was able to move into computational chemistry and work on topics that I wouldn't have imagined a year ago. I have learned a great deal from them over the past year and have been influenced by their contagious love for scientific research. Coming to realize their immense knowledge, I feel very privileged to have gotten the opportunity to work on this masters project under their supervision.

I would also like sincerely thank Matt and Margheritta who I am indebted to. Without their invaluable help, care, guidance and commitment, the project would have looked very differently. They have entirely changed my perception of graduate school where I thought students always face significant obstacles and challenges on their own. The exact opposite was true in this project. I never felt isolated or in need of help that is far away. Their help and patience were so significant. I am truly grateful.

I would also like to thank other members of Dr. Clotilde's group including Celia, Yike and Rashid. I want to thank Rashid especially, who I am very happy to have befriended, for his invaluable advice and help. Our conversations during lunch time will be truly missed.

Last but not least, I would like to thank my family for their support, trust and unconditional love. Without you, none of this would be possible.

## Abstract

Within the expanding forefront of electrochemistry research, computational methods are playing an important role in furthering our atomic-level understanding of various interfaces that are central to devices ranging from fuel cells to nanoelectronics. Such methods allow the resolution of micro-processes, such as charge redistribution, that cannot be resolved experimentally and that could guide rational device design. The complexity of electrode-electrolyte interfaces has rendered the descriptions of even the most fundamental systems namely, metal-water interfaces, incomplete. An effort is made here to *ab initio* molecular dynamics (AIMD) to study a gold junction comprising two electrodes connected by an atom-thick wire, in the presence of water. Such a configuration is relevant to molecular electronic devices, acting as precursors in device fabrication, which show pertinence as devices of ultimate scalability, novel electrochemistry, and computational tractability as a result of the shape and dimensionality of such systems. An understanding of the transformation of the wire in the presence of water and computation of corresponding dynamical electronic states would enable analysis of the molecular scale conductivity of the junction in detail, which would be beneficial for device development.

Density functional theory (DFT) was used to first model bulk gold, followed by gold electrodes. Structural optimization was then run to obtain a meta-stable junction form. The final junction model obtained consisted of 5 electrode layers with 6x6 atoms laterally. Water was then added explicitly to investigate double layer formation and nanojunction dynamics using *ab initio* molecular dynamics (AIMD). Classical MD was then run to obtain an initial water configuration and benchmark results for AIMD. A flexible TIP3P model was used for water and a Lennard-Jones potential was used for gold–water interactions. The favorable configurations of the nanojunction in vacuum and water are compared. For the former, a contracted zigzag-wire shape is assumed, whereas a linear shape persisted in the presence of water for the duration of AIMD. Electronic structures were also analyzed to gain a better understanding of the structural evolution and DL formation. Charge density diagrams revealed that water interacts covalently with the wire atoms through Au-H bonds and predominantly datively with the wire base atoms through Au-O bonds. Bader charge analysis showed that the wire atoms are significantly more negative as a result whereas base atoms are mostly positive. The charge profile across the nanojunction, as well as charge accumulation around the wire atoms were used to tentatively explain the extension of the wire. Finally, projected density of states diagrams showed that the base/tip/wire complex maintains metallic and conductive nature, as well as bonding between the wire atoms amidst the stretched Au-Au bond.

# Contents

<b>1</b>	<b>Introduction</b>	<b>4</b>
1.1	Aims and Objectives . . . . .	6
<b>2</b>	<b>Theoretical Methods</b>	<b>7</b>
2.1	Density Functional Theory . . . . .	7
2.1.1	Many Body Problem . . . . .	7
2.1.2	Born-Oppenheimer Approximation . . . . .	7
2.1.3	Hohenberg-Kohn Theorems . . . . .	8
2.1.4	Kohn-Sham Equations . . . . .	8
2.1.5	Exchange Correlation Functional . . . . .	8
2.2	Numerical Approximations . . . . .	9
2.2.1	Periodic Boundary Conditions . . . . .	9
2.2.2	Bloch's Theorem . . . . .	9
2.2.3	Kpoints . . . . .	10
2.2.4	Basis Sets . . . . .	10
2.2.5	Energy Cutoffs . . . . .	11
2.2.6	Pseudopotentials . . . . .	11
2.2.7	CP2K Package . . . . .	12
2.3	Classical Molecular Dynamics . . . . .	12
2.3.1	Equations of Motion . . . . .	12
2.3.2	Force-fields . . . . .	13
2.3.3	Gold-Water Force-fields . . . . .	15
2.4	Ab initio Molecular Dynamics . . . . .	15
2.4.1	Car-Parinello MD . . . . .	15
2.5	Additional Methods . . . . .	16
2.5.1	Optimizing Lattice Parameters . . . . .	16
2.5.2	Slab Surface Model . . . . .	16
<b>3</b>	<b>Results and Discussion</b>	<b>18</b>
3.1	Bulk Silver and Gold . . . . .	18
3.1.1	Convergence Tests . . . . .	18
3.1.2	Lattice Parameters . . . . .	20
3.1.3	Electronic Structure Calculations . . . . .	21
3.2	Silver and Gold Electrodes . . . . .	23
3.2.1	Slab Vacuum Thickness Convergence . . . . .	23
3.2.2	Convergence Tests . . . . .	24
3.2.3	Slab Layer Thickness Convergence . . . . .	25
3.3	Gold Nanojunction . . . . .	26
3.3.1	Lateral Size Optimization . . . . .	27
3.3.2	Structural Optimization . . . . .	28
3.3.3	Solvation . . . . .	29

3.4	Classical Molecular Dynamics . . . . .	30
3.4.1	NVT Equilibration . . . . .	31
3.4.2	NPT Run . . . . .	34
3.5	Ab initio Molecular Dynamics . . . . .	34
3.5.1	Equilibration . . . . .	34
3.5.2	Water Structure . . . . .	36
3.5.3	Wire Structure . . . . .	38
3.5.4	Electronic Structure . . . . .	39
<b>4</b>	<b>Future Work</b>	<b>45</b>
<b>5</b>	<b>Conclusion</b>	<b>46</b>
<b>A</b>	<b>Appendix</b>	<b>47</b>

# Introduction

The past few decades have witnessed electrochemistry at the core of our most impactful technologies in areas ranging from energy production, storage, electrocatalysis and even nanoelectronics [1]. Devices with prominence of electrochemical effects feature solid/liquid or solid/electrolyte interfaces. Historically, electrochemistry has constantly been a vibrant and exciting area of study, allowing the development of innovative devices such as batteries and fuel cells. EC devices are expected to play a key role in our immediate goals for more sustainable technologies particularly in the energy sector. In the endeavor of realizing high performance EC devices such as batteries or electrolyzers, it is desirable to strengthen our theoretical understanding of fundamental EC processes to enable rational design and accelerate device development which has otherwise been slow. The early period of electrochemistry research featured the proposal of continuum theories, treating the electrolyte as a dielectric, continuous medium, and semi-empirical models, both of which largely neglect atomistic details [2, 3]. Many of these theories have played an important role in intuition-building and rationalization of otherwise inherently complex phenomena. One such central theory that emerged and still maintains centrality and front-end status in electrochemistry is that of the electric double layer (DL).

An electrochemical system is comprised of an interface between an ionic conductor (e.g. aqueous electrolyte) and an electronic conductor (e.g. metal electrodes), with a current typically flowing through. Initial theories of the DL were proposed since the 1850s, based on continuum descriptions and were refined over the years by several researchers including Stern and Helmholtz [4]. When a potential is applied, the charged metal surfaces attract oppositely charged ions in the solution which adsorb onto the surface attempting to neutralize the charge and forming a 'skin' layer referred to as the stationary or Stern layer. The effect of the electric field permeates the first layer and affects surrounding water molecules to form a second less tightly-bounded, diffuse or Helmholtz layer. This is the general description of electrified interfaces that stems from charge anisotropy. However, double layers also occur for generic metal-water interfaces not connected to circuits in the presence or absence of salts and autoionization species (hydronium and hydroxyl ions) [3]. In the latter case (absence), polarization of both the metal and water occur, with water molecules chemisorbing and transferring charge towards the surface, forming structuring around the surface [5]. There is then a minor perturbation to molecules neighboring the first layer, in a loose and diffuse way. The formation of the DL is ubiquitous and is of great importance especially in electrochemistry. Its equilibrium nanostructure and response to an applied potential strongly affect the activation barriers for the mass and charge transfer at electrified interfaces (EIs) which converts chemical into electrical energy and *vice versa* [6].

As with other fields, an interdisciplinary approach has emerged, with cutting-edge computational tools now being applied to deepen our understanding of electrochemistry [7]. Impressive efforts and numerous 'computer experiments' following an electrochemical surface science approach have been aimed at building an atomistic understanding of the various processes and structures occurring at EIs. In spite of these efforts, it is interesting to note that the description of the DL for even common systems such as water/platinum are still debated [3, 6]. This reflects the difficulty of conducting electrochemical studies of relevant theoretical significance. Experimentally, there are a limited number of techniques with atomic resolution that could be used to probe solid/liquid interfaces and the dynamic processes at play. For instance, highly successful solid state characterization techniques based on electron scattering and diffraction cannot be applied as electrons exhibit low penetration depths in water [3]. In techniques that do achieve atomic resolution, such as atomic force microscopes (AFMs), scanning tunneling microscopes (STM) and near field spectroscopy (NFS), there is still the challenge of deconvoluting microscopic details from the average, macroscopic observables.

Amidst the tremendous increase in computer power and speed, computational techniques such as ab initio molecular dynamics (AIMD) have been employed extensively in studying electrochemistry [6]. Computational modelling enables atomic and electronic scale descriptions that can complement experiments. However, there have been serious challenges that hinder the computational approach. Heterogeneous solid-liquid interfaces are inherently complex and necessitate self-consistent theoretical treatment of structure, properties, and reactions at such interfaces [2]. Proper descriptions require explicitly including the electrolyte which in turn demands computationally expensive statistical averaging from AIMD [3]. Moreover, structures and properties of electrified interfaces are governed by the electrode potential, a critical parameter that under the standard canonical framework, cannot be defined and controlled *a*

*priori*, making it hard to compare simulated systems with experiments [3, 6]. These are root causes of considerable complexity when conducting dedicated theoretical electrochemistry investigations in particular. Nonetheless, tangible strides have been made in the field that have allowed for models of increasing realism including methods of directly/indirectly setting the electrostatic potential and studying thermodynamics have been established [6]. This opens up the opportunity for extending the scope of EC systems studied and looking at curious devices with promising applications.

The emergence of nanotechnology has led to the development of electrochemical devices with electrodes separated by no more than tens of nanometres. In such devices, interesting and distinct phenomena occur such as overlapping EDLs in contrast to separated and planar like EDLs in bulk systems. One such device is the electrochemical gate, one of the main configuration of molecular electronic devices [8]. In this system, two electrodes made of gold are bridged by a molecule or ensemble thereof, with a gate that controls overall device conductance. Molecular electronics in general, have attracted considerable interest since their conception in the early 70s [9]. One of the levels of classification in the field is related to the number of molecules bridging the electrodes where two different classes are established: ensemble and single molecular junctions [10]. The interest in ME devices stem from notable hard-to-beat advantages such as low cost, self-assembly properties, low power consumption, multiple conductance states and potentially massive structural variety [9]. Single molecular junctions in particular, are hailed as the ultimate functional devices and have been long sought after.

One of the superior and hence widely applied methods for making and characterizing single molecular junctions is the mechanically controllable break junction (MCBJ) technique developed in 1985 [10]. This is because MCBJs allow comparatively fine control and stability of single molecules. In this technique, electron beam lithography is used to etch a metallic nanowire ( $\sim 10 \times 10 \text{ nm}$ ), typically gold, which is suspended between two electrodes, all of which lie on a substrate [11]. A drop of solvent containing the molecule is added to the system, which is then elongated and bent via a piezo system to break the wire. Followingly, a nanogap forms which is then connected by a few molecules with terminations that are affinitive to the metal, such as dithiol-terminated molecules in the case of gold [11]. Electrical measurements are used to track the different stages of the process including the attachment of the molecules. Upon connection, electrochemical gating, via a gate electrode, may be used to alter the molecular conductance.

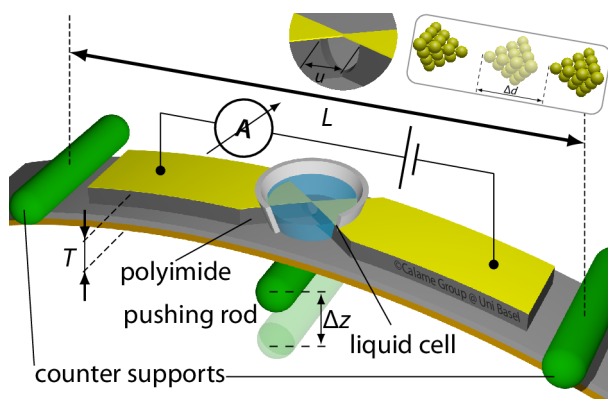


Figure 1.1: Schematic of a molecular break junction [12]

Despite the maturity and superiority of the MCBJ technique, connecting molecules is not always trivial. Lability of bonds and structural reconfigurations are suspected based on current instabilities and telegraphic noise during device operation [11]. In other words, there are elements of variability and randomness similar to other nanoelectronic devices [13]. Understanding such phenomena is naturally difficult due to the spatiotemporal resolution requirements. Interestingly, the solvent and accompanied EC environment play a great role throughout the different stages. For instance, Chen et al. [14] reported an alteration in conductance of a gold nanowire connecting two contact pads resulting from interfacial redox reactions at the gold contacts. Indeed, it was found that  $\text{Ru}(\text{NH}_3)_6^{3+}$  reduction could partially or completely suppress conductance quantization. The observations were attributed to transient oxidation of the Au contact followed by structural relaxations which cause significant changes conductance. Other studies have also shown the effects of molecule-solvent interactions using various solvents with different polarities [15–17]. The dynamics and stability of the nanowire, metal-molecule connects as well as factors influencing conductance should be understood for realization of reliable fabrication and operation,

particularly for large-scale fabrication.

Despite their significance and merits as computationally tractable devices of exciting electrochemistry, there are a few studies that employed AIMD to study nanoelectronic devices and nanoelectrochemistry therein. AIMD modelling MCBJs can be useful in understanding transformations of the wire in the presence of water and computation of corresponding dynamical electronic states would enable analysis of the molecular scale conductivity of the junction in detail, which would be beneficial for device development. It is of interest in this work to make an initiative start in this direction with a simplified model that can be built upon and increased in complexity.

## 1.1 Aims and Objectives

The focus of this work is to model a gold nanojunction, where an atomic wire bridges two electrodes, with water added explicitly. *Ab initio* investigations of water-metal interfaces is quite an active area of research which is still replete with open questions and serves appreciably towards understanding electrochemical systems as will be seen later [3]. One of the interesting features of metal-water systems is the comparable strength of interaction between water-water and water-metal which compete as noted by Groß[3]. The theoretical framework of the model is centred around quantum mechanics, specifically density functional theory (DFT), which is described in detail in the next section. As the system will be restricted to metal-water with no applied bias, first principles electrochemistry is not detailed here.

The reasons for using DFT and AIMD whilst being extremely computationally expensive are manifold. Although water can be described reasonably with classical models, the same is not true for complex metal-water systems. This applies on multiple levels. Firstly, classical models restrict the formation/breaking of chemical bonds during simulations, which are an integral part of DL formation in such systems. In other words, classical models cannot describe the polarization of water-metals and charge transfer, in contrast to QM methods such as DFT [5]. Although there are classical models such as reactive forcefields[18] that bypass this limitation, these often require fitting efforts for the system in hand. The same applies to semi-empirical models. Secondly, it is challenging to describe metals reliably using classical interatomic potentials which are included as approximations of bonds. In the case of dynamic MD simulations where the solvent is expected to exert pressure on an otherwise diffuse atomic wire, classical potentials can lead to quite unrealistic results as will be seen in Section 3.4. However, classical MD (fixing the metal) is used in this work both to obtain an initial guess configuration for water for AIMD.

The objectives of the work are as follows:

- Build a realistic model of a gold nanojunction of reasonable size and structure.
- Run classical MD to obtain a good guess initial configuration for water around a 'relaxed' and realistic gold junction
- Run AIMD for the whole junction and analyse wire dynamics, stability and DL formation.

In summary, the aim of this work is to visualize, using one of the most powerful computational methods in the form of AIMD, DL formation in such a novel system as well as the influence of water on the electronic structure (conductivity) of the wire. The latter is hoped to provide some insight that is hard to resolve experimentally and that could be useful in rationalizing some of the observed behaviours during device fabrication. This is further fruitful as such devices can be reliably and controllably built and studied, which in one rare instance makes it possible to have a tractable atomistic model with quite close resemblance in size to actual devices. Such a model can also be of interest in electrochemical metallization memories (ECM) [19], although they are of larger size (10s of nanometres), setup procedures and insights from solvent-wire dynamics and transport phenomena can be interesting for gaining knowledge on stability and sensitivity factors. In this regard, bulk silver and silver electrodes will also be modelled for future work on ECM devices. Electrochemical sensors, are also an interesting area that can benefit from such a study.

# Theoretical Methods

## 2.1 Density Functional Theory

### 2.1.1 Many Body Problem

Computational modelling is a powerful tool that can be used to understand complex processes occurring at the nanoscale. Among various modelling techniques based on atomistic systems, first principles methods namely, quantum mechanical (QM) methods, are highly versatile as they require minimal inputs. These inputs are as simple as defining the atomic constituents of the system, without any parameterization. Quantum theory is the standard theory at the atomic and sub-atomic levels. The Schrödinger equation lies at the heart of QM. In its time-independent and nonrelativistic form, it describes the spatial wave function ( $\Psi(r, R)$ ) of physical and chemical systems:

$$H\Psi(r, R) = E\Psi(r, R) \quad (2.1)$$

The Hamiltonian  $\hat{H}$ , is the total energy operator, for a system of  $N$  nuclei and  $n$  electrons. The equation has a set of solutions,  $\Psi_n$ , or eigenstates of the hamiltonian. Each of the solutions has a corresponding eigenvalue,  $E_n$  that satisfies the equation.  $\Psi(r, R)$  depends simultaneously on the different bodies in the system and is not distinct for each particle. The detailed Hamiltonian depends on the system in hand [20], however for general systems of interest it acts as an energy operator accounting, among other things, for the total kinetic and potential energies of the system:

$$\hat{H} = \hat{T} + \hat{V} \quad (2.2)$$

$$\hat{H} = \hat{T}_N + \hat{T}_e + \hat{V}_{Ne} + \hat{V}_{NN} + \hat{V}_{ee} \quad (2.3)$$

The fact that the  $\Psi$  depends on the coordinates of  $N$  nuclei and  $n$  electrons simultaneously makes it a high-dimensional variable that can be stored on computer hard drives for only the smallest particles. In other words, there is an exponential scaling relationship with system size. This is referred to as the many-body problem in QM. To extend the utility of the theory, a series of approximations and mathematical theorems have been proposed over the years.

### 2.1.2 Born-Oppenheimer Approximation

One of the earliest attempts at addressing the many-body problem is the BO approximation, which decouples nuclear and electronic motions reducing Equation 2.1 into separate parts: electronic and nuclear wave functions that depend on coordinates of electrons and nuclei independently [21]. This approximation is motivated by the relative mass of the electron to the proton which is more than 1:1800. As the protons are much more massive, nuclei move at different time scales than electrons. Electrons are less spatially localized and thus electronic equations may be solved treating nuclei as point-like structures within the classical limit that fixed at certain positions:

$$\psi(r, R) = \phi(R)\psi(r; R) \quad (2.4)$$

$$\hat{H}_e\psi(r_1, r_2 \dots r_n; R) = E_e\psi(r_1, r_2, \dots r_n; R) \quad (2.5)$$

The ground state energy of a system with  $N$  nuclei at positions  $R_1 \dots R_N$  is then expressed as a function of positions  $E(R \dots R_N)$  which is known as the adiabatic potential energy surface (PES) [20]. Upon obtaining the PES, properties of a system with moving atoms can be obtained using the variational principle. However,  $\Psi_e$  still depends on  $3N$  coordinates for each electron simultaneously. As an example, a storage of  $10^{78}$  TB is needed to compute the wave function of methane [20]. This is still unimaginable.

### 2.1.3 Hohenberg-Kohn Theorems

Alternative routes have looked at reduced, internal variables (or a set of them) that do not depend on all coordinates of the system. Conjugated variables, which are in external control are then found. If one-to-one correspondence, or bijective mapping, between these internal and external variables can be found, one can completely circumvent the necessity to calculate wave functions and all solutions can be expressed in terms of reduced (low-dimensional) internal variables [22]. Any observable can then be determined as a function of the internal variable(s) and the QM problem is solved once a corresponding internal variable is determined. One such method is Density Functional Theory (DFT) where the internal variable is the electron or charge density. DFT was introduced in 1964 by Hohenberg and Kohn in their monumental paper [23]. DFT is underlined by two main mathematical theorems:

- *The ground state energy from Schrödinger's equation is a unique functional of the electron density* [20]. This theorem establishes charge density ( $\rho$ ) as fundamental to addressing the electronic Schrödinger equation by establishing unique, one-to-one correspondence between the ground state density and ground state wavefunction. In other words, the ground state energy  $E$  can be expressed as  $E[n(r)]$ , where the functional form is unknown. This is important as  $\rho$  is a function of three spatial variables.

- *The electron density that minimizes the energy of the overall function is the true electron density corresponding to the full Schrödinger equation* [20]. This second theorem gives us an important feature of the unknown functional form. If it were known, the electron density could be varied until energy is minimized, allowing us to find the correct/relevant  $n(r)$ .

### 2.1.4 Kohn-Sham Equations

With the establishment of the theorems described above by Hohenberg and Kohn, Kohn and Sham developed a mathematical formulations based on the two theorems shortly after, that allow computation of the ground-state properties of a fictitious ansatz of non-interacting particles (in the many-body sense) based on  $n(r)$  [24]. The formulation is in fact an exact mapping of the BO approximated Schrödinger equation. The formulation involves sets of equations each involving single-electron wavefunctions:

$$\left[ -\frac{\hbar^2}{2m} \nabla^2 + V(r) + V_H(r) + V_{XC}(r) \right] \psi_i(r) = \epsilon_i \psi_i(r) \quad (2.6)$$

$V(r)$ ,  $V_H(r)$  and  $V_{XC}(r)$  are three potentials of different forms, the first of which appears in the expanded Shrödinger equation and dictates the interaction between the electrons and the static nuclei. The second is the Hartree potential:

$$V_H(r) = e^2 \int \frac{n(r')}{|r - r'|} d^3 r' \quad (2.7)$$

This potential describes coulombic interactions between individual electrons and a collective charge density of all electrons in the system. Importantly, there is an unrealistic self-interaction component of this potential since the total charge density is constituted by the individual electrons [20]. This error, along with others including those associated with using non-interacting kinetic energies (first term), are lumped into a third potential referred to as the exchange correlation potential,  $V_{XC}$ :

$$V_{XC}(r) = \frac{\delta E_{XC}(r)}{\delta n(r)} \quad (2.8)$$

$E_{XC}$  is a critical variable and is referred to as the exchange correlation functional, which includes unknown terms/corrections. The exact form of this functional is unknown, placing it as one of the major problems in modern physics. Due to the circularity in variable definitions, the Kohn-Sham equations are solved iteratively following algorithms that can be implemented on computers. Once solved, ground state energies can be obtained. This formulation can be applied to study systems consisting of thousands of atoms [20].

### 2.1.5 Exchange Correlation Functional

The beautiful formulation described above is plagued by one critical complication: the form of the exchange correlational functional. The exact form of  $E_{XC}$  is truly unknown. This has opened a major and

active area of research in the quantum chemistry community aimed at approximating this functional in an efficient and accurate manner for different systems [25]. Over the years, a hierarchy of exchange correlational functionals of varying levels of accuracy and complexity have been developed. The most basic is the local density approximation (LDA) which is derived using the free electron gas, which is the only system in which the  $E_{XC}$  can be determined exactly, since  $n(r) = \text{constant}$  [20]. Although simple, this functional has proven surprisingly useful and efficient.

Another class of highly utilized functionals are the general gradient approximation (GGA) functionals in which information on the local density as well as the local gradient in the electron density are used [25]. Indeed, two of the most applied functionals for calculations involving solids are the GGA functionals of Perdew-Wang (PW91) and Perdew-Burke-Ernzerhof (PBE) [20, 25]. In this work, the PBE functional shall be used for solid state calculations (prior to solvation). Upon solvation, vanderwaals dispersion corrections shall be applied for a more reliable description of the structure of water [3]. Indeed, the PBE functional has been shown to 'over-structure' water as evident by resulting radial distribution functions [26]. When VDW dispersion corrections are added, PBEs can provide very good description of water which compares well with experiments [3, 26].

## 2.2 Numerical Approximations

### 2.2.1 Periodic Boundary Conditions

In spite of the establishment of DFT, further computational simplifications need to run simulations of significance to solid state systems. To illustrate the importance of this point, it should be noted that a cubic millimetre of a solid contains more than  $10^{20}$  atoms. This is far beyond our computational abilities. Although devices of interest here have nanoscale dimensions, some parts of the device (electrodes) extend to bulk behaviour/quantities of atoms in directions away from the tips. The standard method of treating solid state systems is by exploiting their symmetry. Solid state materials such as metals are regarded as crystals with regular and periodic arrangements of atoms which can be reduced to unit cells. Unit cells are the most basic repeating units in crystalline structures and consist of lattice points that are invariant under translations. Given information about the unit cell of a structure, namely the lattice motif and cell vectors, it is possible to exploit translational symmetry and map cells onto 3D space to replicate a bulk, perfect crystal [27].

On the computational side, defining a valid, space-filling unit cell allows the use of periodic potentials and periodic boundary conditions (PBCs). The former can be understood by imagining copies or replicas of unit cells surrounding each other such that atomic potentials display periodicity. This further relates to Bloch's Theorem (Section 2.2.2) which can be used to hugely simplify computations. In essence, an artificial simulation unit cell can be created that allows the electrodes to be treated semi-infinitely. Unrealistic effects of finite sample sizes which can be pronounced in electrochemical systems, are also mitigated this way. The task of solving a semi-infinite system is thus condensed to solving the total energy of this supercell.

### 2.2.2 Bloch's Theorem

This theorem was established in 1928, and is of major utility for periodic DFT, where supercells are defined [20, 28]. It applies to the Schrödinger equation as well as the KS equations and states that, translational invariance of the crystal means that the wave functions can only change up to a phase factor under translation:

$$\Psi(r + R_n) = e^{ikR_n} \Psi(r) \quad (2.9)$$

A mathematically equivalent way of stating the prior using Kohn-Sham orbitals, is that the electronic KS-orbitals can be expressed as the product of a lattice-periodic factor  $u(r)$ , which is invariant under translation,  $u(r+R)=u(r)$ , and a plane wave:

$$\psi_k = e^{ikr} u_k(r) \quad (2.10)$$

$k$  is referred to as the crystal momentum and when set as a subscript, is used to characterize wave functions/orbitals. Given the importance of  $k$  – space, or reciprocal space, in QM, we can speak of the

reciprocal lattice of a set of real lattice points, spanned by reciprocal lattice vectors  $b_1, b_2, b_3$ :

$$a_i b_j = 2\pi \delta_{ij} \quad (2.11)$$

$$b_1 = 2\pi \frac{a_2 \times a_3}{\det(a_1, a_2, a_3)} \quad (2.12)$$

Where other reciprocal lattice vectors can be obtained by cyclical permutation of the indices/subscripts [27]. The denominator,  $\Omega = \det(a_1 a_2 a_3)$  is the volume of the unit cell of the lattice in reciprocal space which is called first Brillouin Zone (BZ). Applying PBC, Bloch's theorem is satisfied. Consequently, it will suffice to know  $\psi_k$  within the first BZ solely to determine properties 'bulk' properties. In other words, only information regarding the supercell is needed. This is a dramatic simplification. However, Equation 2.10 needs to be solved for all boundary conditions with k-points in the first BZ [27]. For finite crystals, the number of k-points is equals to the number of unit cells making up the crystal. This means a very large number of k-points is needed in principle, which means computational savings are not promising as of now.

### 2.2.3 Kpoints

In crystals, terms are summed over k-points as mentioned earlier, which in principle, must correspond to the number of unit cells in the crystal. A highly fine sampling is thus required, and due to the size of the sum, it is equivalent mathematically to speak of an integration over the BZ. In practice, there is a weak dependency of the lattice periodic factor  $u_k(r)$  on  $k$ , meaning a finite or relatively small number of sampling points is usually required [27]. Fourier quadratures are used to achieve this numerically, where some lattice periodic function is defined and assumed to be expandable into a finite number of Fourier components. To minimize discretization errors, special k-points are introduced which in the simplest case of simple cubic structure can be envisaged as a homogeneous k-point grid filling the BZ. The number of points on either dimension (or lattice vector) are selected such that sampling is smooth enough for valid integration.

For structures that possess point symmetry, it is enough to simply sample the irreducible, wedge of the BZ since symmetry operations can be used to 'unroll' the full BZ and obtain full information of properties such as charge density and forces [27, 28]. Time reversal invariance can also be exploited even if point symmetries are not present, allows to map the wavefunction  $\psi_k$  to  $\psi_{-k} = \psi^*_k$  provided that magnetization, external magnetic fields or spin-orbit calculations (in a system that lacks inversion symmetry) are applied. This exploitation can reduce the number of k-points by as much as a factor of 2 [27].

The early 70s saw very important research in the setup of k-point grids for computational calculations such as DFT. Efforts were expended to set up economic k-point grids for calculations due to the modest computational power at the time. These techniques include those of Chadi and Cohen [29], and the work of Monkhorst and Pack [30] which are amongst the most common. These are implemented on many of the computational chemistry and physics packages. In this study, the Monkhorst and Pack k-point scheme shall be used. If the grid is dense enough, the error in total energy can be minimized to a few meVs. The optimal grid density shall be determined via convergence tests for respective systems studied.

### 2.2.4 Basis Sets

The discussion of solving and determining wave functions is still not complete. Similar to Equation 2.1 (apart from hydrogen), the wave function in the KS Equation 2.6 cannot be determined analytically. Instead, some functional form needs to be used to describe the wave function which can then be 'guessed' and minimized. Desirably, this functional form should be a good approximation of the true form of wave function. For instance, for a molecule in a vacuum, it is reasonable to assume a localized function. A set of functions summed together may comprise this select functional form for better descriptions (Equation 2.13). Indeed, Basis sets are sets of functions (called basis functions) used to express the KS electronic wave function:

$$\psi_n = \sum_{i=1}^{\infty} |c_i| \psi_i \quad (2.13)$$

where  $\psi_i$  represents a complete set of basis functions. There are different types of basis sets with prevalence depending on the field. In systems that involve periodic crystals with periodic potentials, plane wave (PW) basis sets, which are spatially extended functions, are typically used [20]. Within the framework of Bloch's theorem, PW basis sets can be used to expand  $u_k(r)$ :

$$\psi_k(r) = \sum_G c_{k+G} e^{i(k+G)} \quad (2.14)$$

As  $u_k(r)$  has the same periodicity as the unit cell, the PW basis set are to be summed over all vectors defined by  $G = m_1 b_1 + m_2 b_2 + m_3 b_3$  in reciprocal space. PWs can be converted between real and reciprocal space using fast Fourier transforms (FFTs). They are naturally suited to study periodic systems and are thus the default choice in solid state physics research [20]. Nonetheless, this approach suffers from drawbacks. Atoms along with the vacuum may be described using PWs which means the computational expense can be unnecessarily large.

Conversely, when dealing with isolated molecules as is common the quantum chemistry community, it is natural to use a linear combination of localized functions to approximate the wavefunction/orbitals. There are several forms that can be used here including slater-type orbitals, numerical atomic orbitals or gaussian-type orbitals. The latter (gaussians) are most commonly used due to implementation advantages:

$$\psi_i(r) = \sum_{jlm} C_{ij,lm} e^{-\alpha_i r^2} \hat{Y}_{lm}(\hat{r}) \quad (2.15)$$

The atom-centered nature of the Gaussian approach has obvious disadvantages including insufficiency in describing forces and stresses. However, basis sets in the form of Equation 2.15 are computationally cheap and require small number of coefficients  $C_{ij,lm}$ . In this study the computational package used called CP2K [31], offers a mixed approach referred to as the Gaussian Plane wave method (GPW) that combines advantages of both. The basis sets to be probed in this study that are implementable in CP2K are the MOLOPT-class basis sets which are optimized for metal-molecule interactions. The exact basis set to be used shall be determined via convergence tests.

## 2.2.5 Energy Cutoffs

We can recall that PW basis sets can be used to expand  $u_k(r)$  and consequently the KS wave function as given by Bloch's theorem (Equation 2.14). The application of Bloch's theorem is complemented by the use of k-points over which terms are integrated/evaluated. In its current form, even at a single k-point, solving Equation 2.14 requires the summation of an infinite number of possible values of  $G$ . Fortunately, Equation 2.14 can be interpreted as solutions with kinetic energy [20]:  $E = \frac{\hbar^2}{2m}|k + G|^2$ . It is then reasonable to assume that solutions with lower K.E are more physically important and realistic than higher K.Es and thus the sum can be truncated to a finite series with K.Es lower than a set cutoff value:  $E_{cut} = \frac{\hbar^2}{2m}G_{cut}^2$ . The sum can now be evaluated over terms  $|G + k| < G_{cut}$ . The value of the cutoff energy shall likewise be determined for individual systems through tolerance tests.

## 2.2.6 Pseudopotentials

It is clear from the discussion above, that large energy cutofs should be used when planewaves with short length scale oscillations in real space are desired. Core electrons in atoms are associated with such oscillations, which can be potentially problematic. In conjunction, valence electrodes dominate properties such as chemical bonding and important physical characteristics of materials. A method of approximating the potential of core electrons in a reasonable way, instead of their explicit inclusion in calculations, would be desirable from a computational point of view. The most popular approach to accomplish the aforementioned is the use of pseudopotentials [28]. These are mathematical functions chosen to replace the charge density of core ions with a smoothed density that also captures key physical and mathematical properties of the ions. Pseudopotentials are developed for individual elements and when applied, they replace the core electrons with fixed, approximate properties. The GTH-PBE-q11 pseudopotential found in CP2K's libraries shall be used for the metals.

### 2.2.7 CP2K Package

CP2K is an open source package capable of efficient electronic structure and molecular dynamic simulations for various types of systems [31]. It includes several features and methods implemented including non-equilibrium Green function (NEGF) which is particularly important for nanoelectronics. CP2K is particularly aimed at linear-scaling and parallel electronic structure methods as well as AIMD. The latter is central to this project and due to associated computational costs, choosing the right simulation package is critical. Indeed, CP2K is among the main choices for studying metal-water interfaces amongst researchers [3, 6]. For KS-DFT energy calculations, the Quickstep method can be used. Details on the implementation of the GPW method, MOLOPT basis sets as well as AIMD can be found in the following paper [31]. In this section we will briefly touch on MGRIDs, cutoff and relcutoff which are relevant to the next chapter.

Quickstep makes use of a real-space integration grid, as is the case for most packages, to represent functions such as the product Gaussians and the charge density. A multi-grid system is used for mapping functions such as Gaussians and choosing a fine enough integration grid is critical for obtaining meaningful results. The two key parameters here are the CUTOFF and RELCUTOFF. The CUTOFF keyword controls the PW cutoff (units in Ry) for the finest level of the multigrid, from which the setting for subsequent levels is derived using a progression factor. Conversely, the RELCUTOFF keyword controls the mapping of gaussians onto the grid. Select values of both are to be determined via convergence tests. The Monkhorst and Pack scheme is directly implemented onto CP2K and can be accessed using a keyword.

## 2.3 Classical Molecular Dynamics

Classical MD (CMD) is a highly mature approach that has been employed for decades in various fields of the natural science to probe atomic systems in their fundamental state of constant motion. CMD has been particularly useful in explicit modelling of water in various fields including biochemistry, and is thus implemented on numerous computational packages. In this study, CMD is employed for two purposes: to obtain a good guess configuration of water for AIMD and to obtain benchmark results which AIMD results may be compared against.

### 2.3.1 Equations of Motion

Two important quantities used to define the overall state of a system of  $N$  atoms inside a volume  $V$  are the total kinetic energy (K.E)

$$K = \frac{1}{2} \sum_{i=1}^{3N} m_i v_i^2 \quad (2.16)$$

For atoms with coordinates  $i$ , And the total potential energy (P.E)

$$U = U(r_1, \dots, r_{3N}) \quad (2.17)$$

The universally familiar Newtonian equations of motion are applied to the atoms in the CMD framework:

$$\frac{dr_i}{dt} = v_i \quad (2.18)$$

$$\frac{dv_i}{dt} = -\frac{1}{m_i} \frac{\partial U(r_1, \dots, r_{3N})}{\partial r_i} \quad (2.19)$$

The final equations of motion (2.18 and 2.19) are a system of  $6N$  ordinary differential equations in which energy is conserved ( $E=K+U$ ). In statistical mechanics, such a system naturally evolves within a microcanonical (NVE) ensemble with several possible states and corresponding values of  $N$ ,  $V$ , and  $E$ . Within this framework, temperature is defined using the Maxwell-Boltzmann distribution

$$\frac{k_B T_{MD}}{2} = \frac{1}{6N} \sum_{i=1}^{3N} m_i v_i^2 \quad (2.20)$$

Temperature fluctuates with time in correspondence to the fluctuations in the unconserved K.E quantity. Solving these equations in closed form is extremely complicated, particularly when numerous atoms are involved. A numerical scheme is thus essential. One of the most common numerical techniques to solve these equations is referred to as the Verlet Algorithm [20]:

$$r_i(t + \Delta t) = 2r_i(t) - r_i(t - \Delta t) + \frac{F_i(t)}{m_i} \Delta t^2 \quad (2.21)$$

Equation 2.21 is obtained from the difference of Taylor expansions of  $r_i(t + \Delta t)$  expressed using positive and negative time steps. This algorithm is only accurate for very sufficiently small time-steps. The equations above can be equivalently described using Hamiltonian and Lagrangian mechanics [32].

An important feature of any simulation is comparability with experiments. Under typical experimental conditions, systems are not truly isolated. Instead, devices are able to exchange heat with their surroundings, and exist in thermal equilibrium (constant temperature). In statistical mechanics, systems with constant N,V,T are considered as the canonical (NVT) ensemble. A similar ensemble where pressure is constant is the isobaric (NPT) ensemble which is of interest for systems involving liquids. It is possible to adapt the MD equations including the Verlet algorithm, to mimic a canonical or isobaric ensemble. One possible way of generating these ensembles is to sample sub-spaces of much larger microcanonical ensembles that act as heat baths. However, such an approach is computationally expensive. Instead, thermostat and barostat algorithms are used for the NVT and NPT ensembles to alter classical mechanical behaviour to conform with the ensemble of choice [20]. Such algorithms are numerous, particularly for thermostats [33].

Some of the more well-known thermostats include the Nosé-Hoover, Langevin and canonical sampling through velocity rescaling (CSVR) thermostats [33]. In this work, the NVT ensemble is sampled via the CSVR thermostat, shall be used for obtaining an initial water structure (and velocity distribution) using classical MD. CSVR is a recently developed thermostat that offers efficient implementation without violation of the equipartition theorem as is suspected for simple velocity rescaling [33]. The CSVR operates by rescaling the velocity at time periods defined by TIMCON (e.g. 100 femtoseconds) by a factor  $\lambda$  such that kinetic energy exhibits the distribution of the canonical ensemble.  $\lambda$  is of the form [33]:

$$\lambda = \left( \frac{K_{target}}{K} \right)^{1/2} \quad (2.22)$$

where  $K_{target}$  is drawn stochastically from the probability density function:

$$P(K_{target}) \propto K_{target}^{\frac{N_{DOF}}{2} - 1} \exp(-\beta K_{target}) \quad (2.23)$$

### 2.3.2 Force-fields

During every time step  $\Delta t$ , the force acting on each particle of coordinate i,  $F_i(t)$ , is re-evaluated. The force is given by the derivative of the total potential energy U. Force-fields are used to describe the functional forms of potentials experienced by atoms in vicinity of each other and are thus central to CMD simulations. Not only does the force-field model govern the accuracy and meaningfulness of structures and dynamics obtained during simulations, it also dominates computational time and thus needs to be selected wisely. A vast amount of water models have been developed in the past decades with varying performance, complexity, parameterization and computational efficiency [26]. The term 'water model' here is intended to capture the complete set of force-field parameters related to running MD simulations of water including bond angles, lengths, force constants and atomic partial charges.

In general, water models differ in three main aspects; (1) the number of interaction points called sites, (2) whether the model is rigid or flexible, (3) whether the model includes polarization effects. Simulations of water began in the early 60s, however models that still persist today were first introduced in the 80s [26]. The first class of water models were the 3-point models, which include the simple point charge model (SPC), in which water was modelled using simple geometries. These models are computationally cheap to run and maintain adequate relative accuracy. A wide range of models have been developed further over the years including force-fields based on *ab initio* potential energy surfaces, 4-point models and polarizable models [26]. Currently, there is no single water model that captures all experimental properties of water (under all conditions). Instead, some water models are better at, frequently by design, reproducing certain properties compared to others.

It is of interest here is to get a good initial guess configuration for AIMD where bulk density and important structural features are reproduced in a relatively short period of time. Therefore, it suffices to use one of the class I models (3-point models) which are implemented on CP2K already and are computationally efficient. A flexible Transferable Interaction Potential 3-point model (TIP3P) model shall be used in this work [34]. This is part of the class I models developed early on, and is modified to allow for flexibility of the bond angles:

$$H = \sum_i \frac{p_i^2}{2m_i} + \frac{1}{2} \sum_{bonds} k_b(b - b_0)^2 + \frac{1}{2} \sum_{angles} k_\theta(\theta - \theta_0)^2 + \sum_{i>j} \frac{e_i e_j}{4\pi\epsilon_0 r_{ij}} + \sum_{i>j} 4\epsilon_{ij} \left[ \left( \frac{\sigma_{ij}}{r_{ij}} \right)^{12} - \left( \frac{\sigma_{ij}}{r_{ij}} \right)^6 \right] \quad (2.24)$$

$b_0$  and  $\theta_0$  are reference values for bond lengths and angles respectively,  $k_b$  and  $k_\theta$  are related force constants,  $e_i$  denotes the charge of the  $i^{th}$  atom,  $\epsilon_0$  is the dielectric constant in vacuum,  $r_{ij}$  is the distance between the  $i^{th}$  and  $j^{th}$  atoms, and  $\sigma_{ij}$  and  $\epsilon_{ij}$  are constants of the Lennard-Jones potential. Values of the parameters of the model are found in Table 2.1. A small vanderwaals radius is also given to each hydrogen atom to prevent the 'electrostatic catastrophe'.

**Table 2.1:** Parameters of the flexible TIP3P model for water used in this work [34]

Parameter	Value
$b_{OH_0} = b_0$	0.9572 Å
$\theta_0$	104.52 deg
$k_{b_{OH}} = k_b$	900 $\frac{kcal}{mol^2}$
$k_0$	110 $\frac{kcal}{mol rad^2}$
$e_{H_1} = e_1$	0.417 $\epsilon_0$
$e_O = e_2$	-0.834 $\epsilon_0$
$e_{H_2} = e_3$	0.417 $\epsilon_0$
$\sigma_{OO}$	3.1507 Å
$\sigma_{HH}$	0.40 Å
$\epsilon_{OO}$	-0.152073 $\frac{kcal}{mol}$
$\epsilon_{HH}$	-0.04598 $\frac{kcal}{mol}$

Now that water-water interactions are defined, the next important set of interaction potentials to be defined are those of Au-O and Au-H, as part of defining gold-water interactions. There are several functional forms that could be used for such interatomic potentials including basic models such as the Lennard-Jones (LJ) potential [35]. Ultimately, these are non-bonded interactions and over the course of standard classical simulations, no chemical reactions i.e., bond breaking/formation occur, in contrast to AIMD. Nonetheless, it is possible to approximate AIMD water properties such as orientation of the molecules and proximity to metal surface using classical models that are fitted against DFT simulations of water on gold. Berg et. al [35] fitted different classical models including LJ, Buckingham and Morse potentials to results of DFT simulations on gold. After parameterization, the models could reproduce features of the structure of water on gold found in DFT simulations. The DFT-parameterized 12-6 LJ potential from their work is used in this study as this potential is implemented on CP2K:

$$V_{LJ}^{12-6}(r_{ij}) = \epsilon_{ij} \left[ \frac{1}{2} \left( \frac{r_m}{r_{ij}} \right)^{12} - \frac{1}{2} \left( \frac{r_m}{r_{ij}} \right)^6 \right] \quad (2.25)$$

where  $\epsilon_{ij}$  is the energy at the equilibrium distance  $r_m$ . The familiar zero energy,  $\sigma$ , can be obtained from  $r_m$  as follows:

$$\sigma = \frac{r_m}{2^{1/6}} \quad (2.26)$$

Equation 2.25 is implemented on CP2K and only requires input values for the parameters. These are given in the Table 2.2 below.

**Table 2.2:** Parameter values of the Lennard-Jones equation for gold-water interactions [35]

pair	$\epsilon_{ij} \frac{kJ}{mol}$	$r_m(nm)$
Au-O	3.61	0.318
Au-H	0.01	0.395

### 2.3.3 Gold-Water Force-fields

It can be noticed that Au-Au interactions were not defined in Table 2.2. Initial CMD simulations will have gold atoms fixed, requiring no Au-Au interactions to be specified. However, in the interest of getting the density of water right, NPT runs are attempted. In such an ensemble, the unit cell (and gold atoms within) need to be dynamic, necessitating the specification of Au-Au interactions. In the early days of MD simulations, simple pair-potentials were used to describe atomic interactions and enable the simulation of large systems in line with the modest computational power at the time. However, it was shown that such potentials are incapable of describing metals even qualitatively [36]. Attempts to describe metal-metal interactions classically resulted in the development of the embedded atom method (EAM). The EAM model was able to overcome many of the failures of earlier classical models and several models following the same mathematical framework were developed such as the Glue model [36]. Gold is a common metal in many applications that are simulated using CMD such that several dedicated Au-EAM models have been developed over the years [36, 37]. Exact details of EAM models are not covered here. In simulations that require an Au-Au potential, a parameterized POT file compatible with CP2K will be used [38].

## 2.4 Ab initio Molecular Dynamics

In the previous section, it was shown that the dynamics of atoms and molecules could be described provided that the potential of atoms,  $U = U(r_1, \dots, r_{3N})$  is known as a function of atomic positions. It was also shown that in classical MD, parameterized force-fields (or models) of various sorts are defined to supply the information on potentials. A natural question arises, is it possible to calculate  $U = U(r_1, \dots, r_{3N})$  with DFT and perform molecular dynamics? In other words, can we not use quantum mechanics to calculate potentials "on the fly"? After all, nuclei trajectories can be advanced by using classical mechanics with forces calculated using DFT. This is indeed the concept of *ab initio* molecular dynamics (AIMD).

### 2.4.1 Car-Parinello MD

Despite the attractiveness of this method, in that the benefits of first principles methods may be realized in dynamic simulations, we have seen that very short time steps are required for MD algorithms. Considering the computational costs of running even single point energy calculations using DFT, the usefulness of this concept may seem doubtful. It was the fruitful efforts of Car and Parinello that first enabled the practical application of this concept [39]. The initial formulations of AIMD imposed carrying out the calculations sequentially, with ground-state energies evaluated first, followed by advancing nuclei positions through one step of MD [20]. Car and Parinello were able to develop an algorithm, following an extended Lagrangian, that unifies the separate tasks of calculating ground state energies and advancing nuclear positions:

$$L = \frac{1}{2} \sum_{i=1}^{3N} m_i v_i^2 - E[\varphi(r_1, \dots, r_{3N})] + \frac{1}{2} \sum_j 2\mu \int d\mathbf{r} |\psi_j(\mathbf{r})|^2 + L_{ortho} \quad (2.27)$$

where  $\varphi(r_1, \dots, r_{3N})$  represents the full set of KS single-electron wave functions whereas the last two terms on the right-hand side introduce fictitious degrees of freedom. In more detail, the third term involves a fictitious mass  $\mu$  and is in the form of kinetic energy, while the final term imposes orthogonality onto the KS wave function [20]. The configuration in which an energy minimum (equilibrium) is reached when associated velocities are scaled such that  $T \rightarrow 0$ , corresponds to a physically real system occurring on the PES. This method, which is referred to as Car Parinello MD (CPMD) is implemented on CP2K and is used in this study [31].

Some additional changes to be made when running AIMD. As mentioned in the introduction, the GGA-PBE functional does not describe water well and results in over-structuring of water as demonstrated by several studies. A way to overcome this is to include vanderwaals dispersion interactions. This has shown to significantly improve the water structure and properties when using the PBE functional [3]. The orbital transformation (OT) method will be employed to speed up the SCF convergence.

## 2.5 Additional Methods

With multiple theories and core methods defined, it is necessary to outline the steps or order followed in this work along with other important methods or theories not covered yet. In the previous sections, basis sets, k-points, Cutoff and Relcutoff were defined. The optimal setting for each is to be determined using convergence tests where the difference in the value of variables, particularly total energy, are compared for different settings of a certain simulation parameter. In this work, it is necessary to simulate both bulk gold and surface/slab gold models as it is intended to build a junction with elements of both. Silver will also be modelled along with gold, except for the junction, with future aims to model ECM devices [19].

### 2.5.1 Optimizing Lattice Parameters

It is standard to start by modelling the bulk metals. To do so, conventional FCC unit cells of both silver and gold will be defined using four metal atoms and starting with the experimental value for the lattice constant  $\alpha$ . Convergence tests will be conducted for selection of simulation parameters. Followingly, it is necessary to find the optimal  $\alpha$  value that minimizes the total energy with respect to the optimal simulation parameters. This is necessary for two reasons: firstly, failure to determine a 'relaxed' bulk metal unit cell means that there will be residual forces acting on the system during subsequent calculations. Secondly, the  $\alpha$  value corresponding to the simulation setup can be compared with experimental values and that of other DFT calculations to validate the setup. To find the optimal lattice parameter, the Murnaghan Equation of state can be used [40]:

$$E(V) = E_0 + \frac{K_0 V}{K'_0} \left( \frac{(V_0/V)^{K'_0}}{K'_0 - 1} + 1 \right) - \frac{K_0 V_0}{K'_0 - 1}. \quad (2.28)$$

The total energy will be calculated for different  $\alpha$  values and thus unit cell volume volumes (V). Equation 2.28 can then be fitted against the results to obtain the  $\alpha$  (from  $V_0$ ) corresponding to  $E_0$ . Next, electronic structure calculations will be run to obtain the band structures and projected density of states (PDOS) of both silver and gold. This may serve as a final validation of the simulation setup.

### 2.5.2 Slab Surface Model

Next, the junction electrodes need to be modelled. The electrodes shall be based on the Au and Ag 111 surfaces which are the most stable surfaces and thus most likely to be found in nature [41]. Moreover, electrodes are to be modelled semi-infinitely (infinite in the lateral directions upon applying PBC) and approach bulk behavior in the middle layers meaning, the surface layers of the electrode should be decoupled from the connected surface of the periodic copy. It is therefore necessary to determine the optimal number of layers making up electrodes (considering periodic copies). For this, the electrodes need to be modelled individually. The slab geometry is often employed for this purpose when working with PBCs [27].

A slab is simply a stacking of layers of certain crystallographic planes/facets with surfaces exposed on either end. Similarly to surfaces, slabs are aperiodic in the direction perpendicular to the surface. To maintain overall periodicity and make use of Bloch's theorem, vacuum layers can be added on either surface, to create a supercell (slab + vacuum) which could be subjected to PBC. Vacuum layers, if selected thick enough, can prevent interactions of slabs with their copies in the direction perpendicular to the surface. Otherwise, the total energy of such a unit cell will diverge due to an infinite number of coulomb interactions between periodic copies. Therefore, before determining the optimal number of layers, it is necessary to determine the optimal vacuum thickness. Orthogonal 2x2x1 layers slab unit cells will be used in this part of the study, built using ASE and the 'relaxed' lattice parameter from bulk calculations for

initial configurations. With the introduction of surfaces, we can now also probe the work function  $\Phi$  of the slab. Similarly to the bulk case, some convergence tests will be conducted for slabs considering both  $E_{tot}$  and  $\Phi$ .

The surface formation energy  $\sigma$ , and the work function  $\Phi$  can be used to determine the optimal number of layers in the electrode.  $\sigma$  is the (reversible) work done in creating a crystal surface of given unit area [42]:

$$\sigma = \lim_{N \rightarrow \infty} \frac{1}{2A} (E_{slab}^N - NE_{bulk}) \quad (2.29)$$

Where  $E_{slab}^N$  is the total energy of a slab, of cross-sectional area A and layers N. The fraction  $\frac{1}{2}$  accounts for the presence of two surfaces. This intuitive procedure singles out the contribution of a surface. If the slab is too thin, upper and lower surface may interact (no bulk behavior in between), causing their energetic contributions to deviate from the surface energy of a semi-infinite slab. Semi-infinite and thus intermediary bulk behavior can be reproduced by increasing the number of layers N until  $\sigma$  converges. Depending on the material, N is typically around 5 to 15 layers [42]. Different methods have been proposed in the literature for computing Equation 2.29, as direct implementation using an  $E_{bulk}$  value from a separate calculation, despite similar parameters, may result in divergence. One method proposed is that of Fiorentini and Methfessel [42], where results of  $E_{slab}^N$  for different values of N can be used to estimate  $E_{bulk}$ :

$$E_{slab}^N \approx NE_{bulk} + 2A\sigma \quad (2.30)$$

Equation 2.30 above approximates Equation 2.29 and allows extraction of  $E_{bulk}$  as the gradient of the plot of  $E_{slab}^N$  against N. Such a linear approximation holds very well for thin slabs and at worst, is off by a few milli-Rydbergs [42]. Upon obtaining  $E_{bulk}$ , Equation 2.29 can then be used to describe  $\sigma$ .

In addition to  $\sigma$ , it is also important for the application in hand to study the work function  $\Phi$ . Formally,  $\Phi$  is the minimum energy required to extract an electron from the surface to an infinite distance away from the surface:  $\Phi = [V_{el}(+\infty) + E_{N-1}] - E_N$ , with  $V_{el}(+\infty)$  being the electrostatic potential far away from the surface and  $E_{N-1}/E_N$  the total energies of the surface with N-1 and N electrons respectively. As demonstrated by Lang and Kohn [43], this is equivalent to:

$$\Phi = \Delta V_{el} - E_F \quad (2.31)$$

The average electrostatic potential,  $V(x,y,z)$ , is given as an output in DFT calculations. A two step process is usually taken to extract electronic energy related properties including  $\Phi$ , from  $V(x,y,z)$ . Firstly, the planarized average,  $V(z)$ , in the direction perpendicular to the surface is obtained. A constant is used to scale the electrostatic potential energy such that its reference or zero value is in the vacuum [42]. Next, the macroscopic average in the z-direction,  $\bar{V}(z)$  is calculated considering the interplanar spacing (d);  $\bar{V}(z) = \frac{1}{d} \int_{-d/2}^{d/2} V(z+z') dz'$ . Since  $V(z)$  is periodic within the slab, it is expected that  $\bar{V}(z)$  would assume a constant value thence. Followingly,  $\Delta V_{el}$  is set equals to  $\bar{V}(z)$  in the middle of the vacuum which is taken as the point of infinite separation from the surface used to define  $\Phi$  [42].

After determining the number of layers for the electrode, the junction can be set up by bridging two electrodes with tips connected by an atomic wire. The tips will lie on either electrode and be composed of three atoms in a triangular pattern with the atoms on end of the wires starting from the vacancy in the middle of the tips. The electrodes as well as tips should follow the stacking symmetry of the FCC 111 planes (ABCABC..) for the purpose of PBC. The junction will then be structurally optimized using cell optimization (CELL OPT) where the unit cell will be allowed to relax in the C plane in addition to the atomic re-arrangements of geometry optimization. Next, the junction is solvated by carefully calculating the exact volume available for water atoms. Classical MD using the NVT ensemble is run, keeping the gold atoms fixed to get a good initial guess for water structure. Classical NPT is then attempted (restricting cell movement to the c plane) to ensure we have the correct liquid density. Finally, AIMD can be run after ensuring the correct water density is obtained.

# Results and Discussion

## 3.1 Bulk Silver and Gold

### 3.1.1 Convergence Tests

The first steps for running theoretical calculations are typically convergence tests which are done to provide benchmark values for important simulation parameters. Obtained parameter values can then be used to extract lattice parameters corresponding to energy minima with respect to the simulation parameters and proceed with electronic structure calculations. A criterion of  $5\text{meV}$  in difference with respect to the most accurate simulation parameter setting (defined as error) will be used for determining the optimal simulation parameter. The results in this section are shown side by side for silver and gold.

#### Basis sets

Basis sets selection has a heavy impact on accuracy limits and computational costs. As described earlier (reference theory), MOLOPT basis sets which are optimized for metal-molecule interactions are tested for both silver and gold. Specifically, the following basis sets are tested: **SZV-MOLOPT-GTH**, **DZVP-MOLOPT-GTH**, **TZVP-MOLOPT-GTH** and **TZV2P-MOLOPT-GTH** [31]. These stand for single, double and triple zeta polarized basis functions. The aforementioned include individual sets of polarization functions with the exception of the TZV2P basis set which has two. Generic values are set for other parameters such as cutoff, for the different basis set single point runs. The errors in total energy are defined with

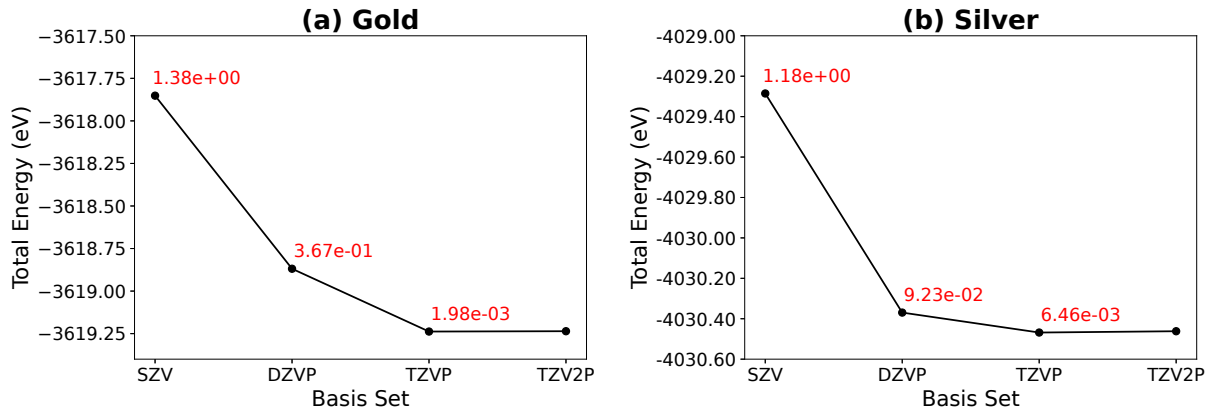


**Figure 3.1:** Basis sets convergence test for Au and Ag , Cutoff=300Ry, Relcutoff=40Ry, k-points=8x8x8, with errors in red

respect to the most robust basis set, the double polarized triple zeta basis set (TZV2P) and are annotated above data points in red. The Figure 3.1 above shows that the TZVP basis set is on the order defined for the error criterion for silver and is met for gold. Interesting differences between the two such as the relative efficiencies in the DZVP can be observed, but these are not discussed further here. Considering the computational expense of the TZV2P basis set, the TZVP is sufficient for use for both silver and gold.

#### Cutoff

The PW cutoff is a very important parameter for periodic metallic systems. A cutoff range of 150 Ry to 550 Ry is tested for both silver and gold.

Lower cutoff values are required to converge  $E_{tot}$  for gold compared to silver. Since the final system will involve molecules, a cutoff of 300 Ry is a necessary minimum, which also corresponds to negligible error for the two metals.

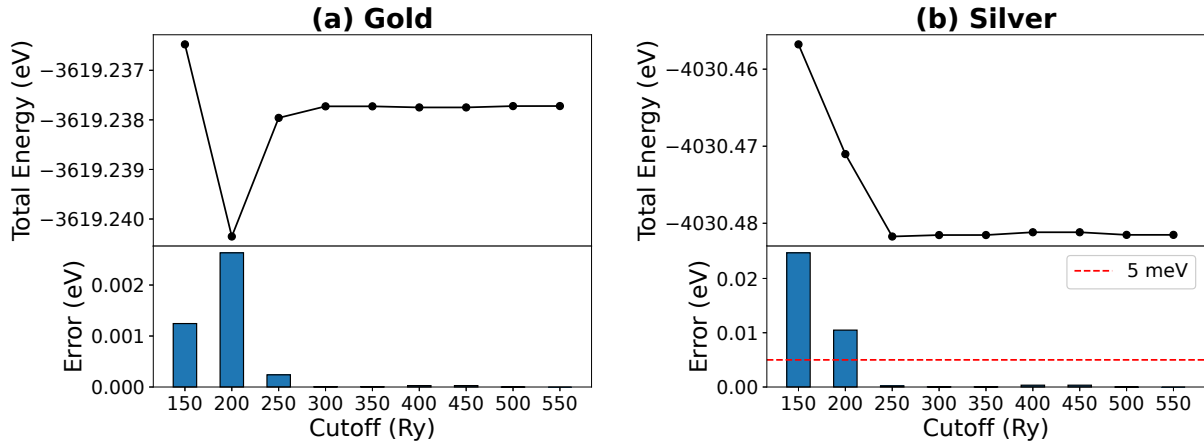


**Figure 3.2:** Cutoff convergence test for bulk Au and Ag using basis set=TZVP, Relcutoff=40Ry, k-points=8x8x8

### Relcutoff

The relcutoff is a parameter which is typically kept at the default value (40 Ry). The relcutoff was varied from 20 to 100 Ry, where the  $E_{tot}$  value at 100 Ry was used at the benchmark for accuracy.

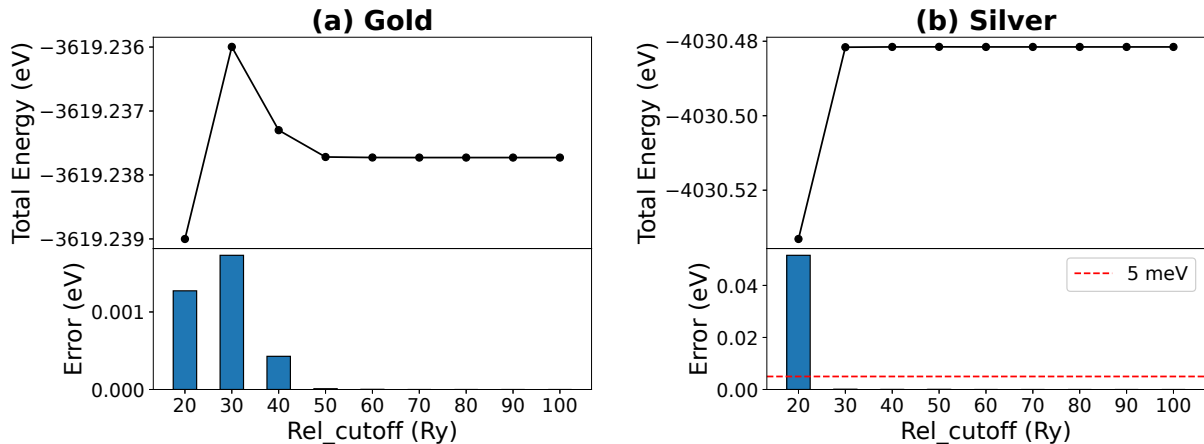


**Figure 3.3:** Relcutoff convergence test for Au and Ag, basis set=TZVP, Cutoff=300Ry, k-points=8x8x8

Relcutoff inputs converge  $E_{tot}$  very well. The default value (40 Ry) is indeed enough to attain negligible errors.

### K-points

Selection of K-points ( $k_x, k_y, k_z$ ) depends on the geometry of the supercell/system being modelled. For unit cells that are orthogonal, even-numbered k-points should be used in order to have a  $\Gamma$ -centered k-point grid which is more efficient [30]. The unit cell used for the bulk metals is the FCC cubic conventional cell, therefore  $k_x = k_y = k_z = N$ . N is varied from 6 to 20 for both metals, using only even numbers, with N=20 acting as the benchmark for accuracy.

Judging by Figure 3.4, N=8 appears to be the first value that meets the error threshold, however this selection appears to be an outlier and is expected to be insufficient for slabs. The next value that meets the criterion (N=14) is therefore used for further simulations.

The optimal selections for the main four simulation parameters coincide for silver and gold and are summarized in Table 3.1

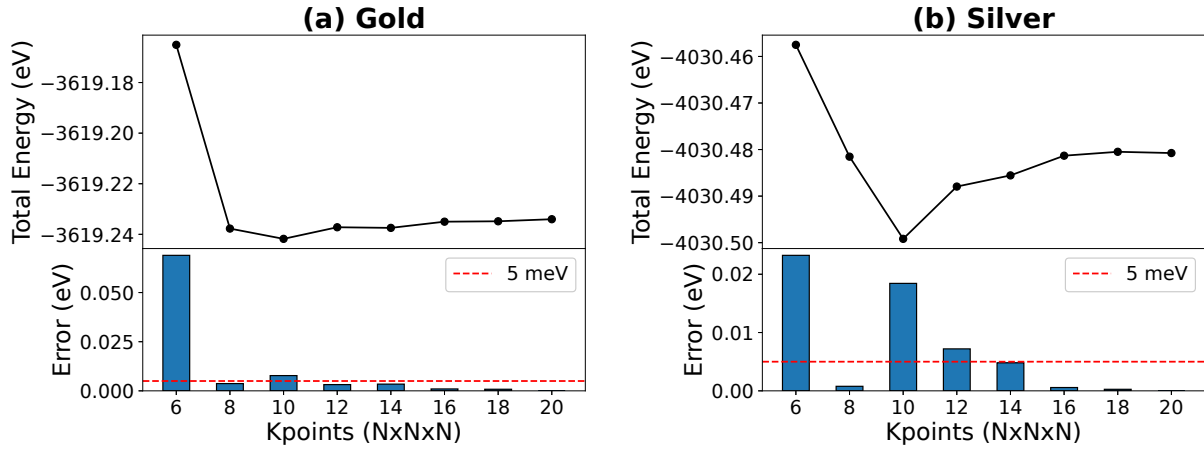


**Figure 3.4:** k-points convergence test for Au and Ag, basis set=TZVP, Cutoff=300Ry, Relcutoff=40Ry

**Table 3.1:** Optimal selections for simulation parameters following convergence tests

	Basis set	Cutoff (Ry)	Relcutoff (Ry)	K-points (NxNxN)
Au	TZVP-MOLOPT-GTH	300	40	14x14x14
Ag	TZVP-MOLOPT-GTH	300	40	14x14x14

### 3.1.2 Lattice Parameters

The lattice parameters ( $\alpha$ ) corresponding to the optimal simulation can be obtained by running single-point energy simulations using different  $\alpha$  values and fitting against equation.  $\alpha$  was varied over  $\pm 5\%$  the experimental  $\alpha$  values of silver and gold which are  $4.0853\text{\AA}$  and  $4.0782\text{\AA}$  respectively.

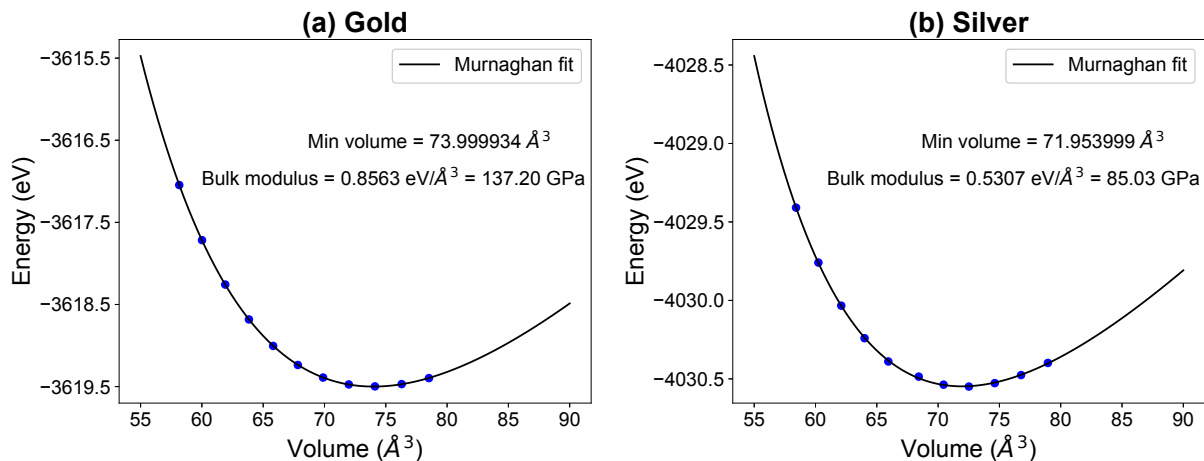


**Figure 3.5:** Fitting the Murnaghan EOS using  $E_{tot}$  values for (a) Au and (b) Ag

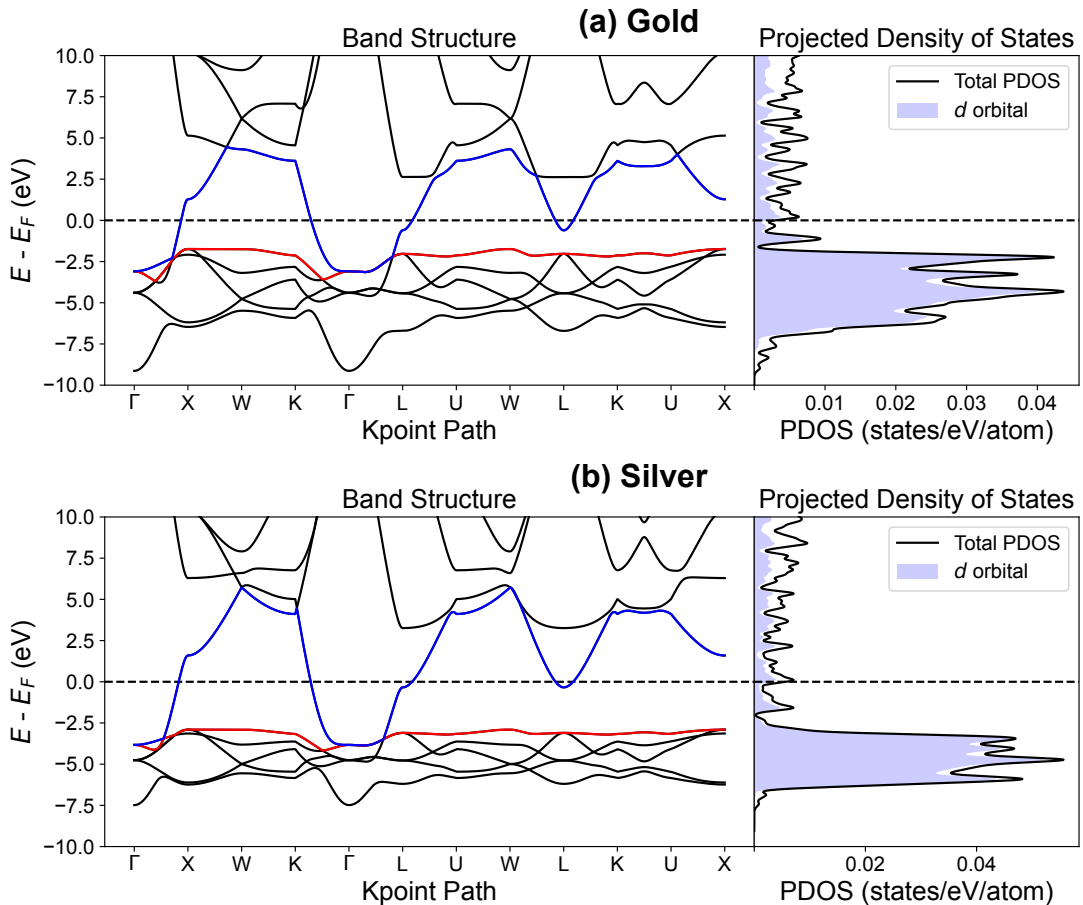
From Figure 3.5,  $\alpha_{Au} = 4.1983\text{\AA}$  and  $\alpha_{Ag} = 4.1592\text{\AA}$ . The bulk moduli ( $\beta_0$ ) also appear in the Murnaghan EOS and are evaluated as  $1.372\text{Mbar}$  and  $0.850\text{Mbar}$  for Au and Ag respectively. Both parameters can be compared to experiments as well as other DFT calculations employing GGA functionals (e.g. GGA-PBE). Table 3.2 shows values for  $\alpha$  and  $\beta_0$  from various sources. For both Au and Ag,  $\alpha$  is overestimated compared to the experimental values. This is common for the GGA-PBE functional as evident by results of other GGA-simulations. For both metals, the  $\alpha$  values are similar to those obtained from other DFT-GGA calculations, validating the simulation setup.  $\beta_0$  on the other hand, is underestimated for both metals and for other simulations partly as a consequence of the overestimated  $\alpha$  values.

**Table 3.2:** Optimized values of  $\alpha$  and  $\beta_0$  of Au and Ag compared to other sources

Source	$\alpha$ ( $\text{\AA}$ )			$\beta_0$ ( $M\text{bar}$ )		
	Experiments	GGA-simulations	Results	Experiments	GGA-simulations	Results
Au	4.0782 [44]	4.1750–4.190 [45–48]	4.1983	1.740 [48]	1.320–1.450 [45–49]	1.372
Ag	4.0853 [50]	4.1540 [50], 4.1590 [48]	4.1592	1.038 [48]	0.833 [48], 0.89 [50]	0.850

### 3.1.3 Electronic Structure Calculations

The band structures and PDOS of both metals can be obtained using CP2K. In the case of the band structure, it is necessary to define high-symmetry paths (band lines) corresponding to the unit cell being simulated. Some handy online tools have been developed over the years that produce reliable and optimized k-space paths for a given input structure [51]. The complete k-space path for FCC metals used for calculations on the Aflow website was adopted here for both metals [52]. The k-path is as follows:  $\Gamma - X - W - K - \Gamma - L - U - W - L - K | U - X$ . The number of points between each high-symmetry point was set as 500 and the simulation was run using the parameter values in Table 3.1. As for the PDOS, CP2K does not have the capability to produce PDOS information when k-points are enabled in DFT calculations (Quickstep). An alternative method to maintain the equivalence of using k-points is to use the *supercell* keyword. There is a linear relationship between the size of the supercell (or unit cell) and the k-points required [27]. For instance, a calculation on a unit cell using  $k_x, k_y, k_z$  k-points, and that on a supercell of  $k_x \times a, k_y \times b, k_z \times c$  larger than the unit cell without k-points are equivalent. This linear relationship shall be revisited for slabs.

**Figure 3.6:** Band structure and PDOS for bulk (a) Au and (b) Ag

For the purpose of obtaining PDOS, using a  $14 \times 14 \times 14$  supercell of the conventional unit cell would be prohibitively expensive (10,976 atoms). Instead, a compromise is made here and an  $11 \times 11 \times 11$  supercell of the 1-atom, primitive unit cell of each metal is used to obtain PDOS information.  $11 \times 11 \times 11$

was selected after building up with smaller supercells ( $4 \times 4 \times 4$  and  $8 \times 8 \times 8$  using a primitive cell and  $6 \times 6 \times 6$  using a conventional cell) until observed changes to the PDOS output were minimal indicating proximity to bulk behaviour.

Figure 3.6 shows the band structure and PDOS for both metals with a shared y-axis. Band structures depict on a 2D plot, information on the allowed energy levels of electrons when propagating in certain key directions in crystals based on high-symmetry points. These energy 'bands' are compact ways of representing information that would otherwise require 4D plots [20]. PDOS on the other hand, can be defined as the number of electron states with energies in interval  $(E, E + dE)$  and can be obtained in periodic-DFT by integrating the resulting electron density in k space. The fermi level, the highest occupied energy level at  $T=0$  K, was set to zero ( $E - E_F$ ). Beginning with the band structure for gold, it should be noted that this has been an open area of research for several decades [53–55]. Early studies in the seventies focused on including relativistic effects into band structure calculations, which are responsible for gold's unique colour [53]. A wide range of DFT functionals and *ab initio* methods (e.g. many body perturbation theory) have been applied to get theoretical band structures that reliably reproduce experimental results [55]. The band structure for gold obtained here agrees quantitatively with other GGA-PBE simulations that do not include relativistic effects [55, 56]. However, there are disagreements with experimental results (quantitative) which are common to GGA-PBE simulation in general [57]. Notably, the interband gap, between the highest occupied 5d band (red) and the lowest unoccupied 6sp bands (most immediate band above the fermi level, the first of which is drawn in blue), is underestimated by over 1eV. Accounting for relativistic effects typically improves the interband gap underestimation to around 1 eV [55]. In general DFT (the GGA functional inclusive) fails to quantitatively underpin band gaps [57]. For the purpose of this study, it is not critical to quantitatively describe the band structure. Otherwise, the recent method pioneered by Rangel et. al [55] based on many-body perturbation theory can be applied. As for the PDOS of gold, this is in agreement with experiments and theory in terms of the energy range at which the DOS are concentrated, the non-zero DOS at the fermi energy (metallic conductor) and the dominance of the d-orbital (5d) towards the total DOS, which is comprised of components (outer s, p, d, f orbitals) [58].

As for silver, the band structure is in good agreement with other GGA simulations and with experiments, qualitatively [56, 59]. Important features are resolved, giving credence to the simulation parameters (as well as the k-path scheme). Similar to gold, there is an underestimation of the interbandgap resulting from the GGA-PBE functional. In the case of silver, quasiparticle corrections have been applied to DFT eigenvalues with great success, leading to remarkable agreements with experiment [55]. As mentioned earlier, it is not necessary in this study to exactly underpin the electronic structure of the metals. The PDOS of silver, like gold, greatly resembles that of other DFT simulations [20]. The energy range and relative densities in the PDOS of silver are well reproduced validating the model.

In summary, a series of convergence tests for important simulation parameters were conducted for bulk silver and gold with the aim of optimizing accuracy vs computational time. This is a necessary step for modelling the electrodes via the slab geometry. The lattice parameters and electronic structures are in good agreement with other DFT-GGA calculations, validating the simulation setup. The next section will look at modelling silver and gold electrodes, and is commenced with some convergence tests in which the tests conducted in this section as well as the lattice parameter, will be used as initials.

## 3.2 Silver and Gold Electrodes

Although convergence tests were already conducted for the bulk metals, it is necessary to build on those tests with further tests on slabs for several reasons. Firstly, the supercell now consists of vacuum regions on either end of the slabs which is expected to change the cutoff requirements (higher cutoff) to maintain the same accuracy. Moreover, the system geometry of and number of atoms now differ, meaning k-point sampling requirements will also differ. The supercell has the geometry of a rectangular prism, meaning the simplistic  $k_x = k_y = k_z$  mesh is not satisfactory. In the case of slabs  $k_z = 1$  is used for two reasons. The supercell  $a_3$  (or  $C$ ) vector is usually large for slabs, meaning the reciprocal counterpart  $b_3$  is short. Secondly, for thick enough vacuum layers (which will be established in the next subsection) there is minimal electronic dispersion in the  $a_3$  direction, making it possible to obtain accurate results using only a single k-point [20]. Although the supercell vectors  $a_1$  and  $a_2$  are not equal, they are similar and thus the mesh will be of the form  $k \times k \times 1$  where  $k$  will be determined. Another reason for further convergence tests, is to investigate changes in a variable of relevance to surfaces, and that is the work function  $\Phi$  introduced in Section 2.5.2. This may change requirements altogether. Hence, convergence tests will be repeated for both cutoff and the k-point since the relcutoff and basis-sets choice should not be impacted. 2x2x3 supercells will be used for the convergence tests to save on computational time. Prior to that, it is necessary to establish an optimal slab vacuum thicknesses in which the electron density tails off to zero and periodic copies are decoupled. In the case of slab calculations, all runs are geometry optimizations (GEO OPT) where the whole structure 'relaxes', finding an energy minimum. The absolute middle layer (or layers for even-numbered slabs) are fixed to bulk positions to artificially enforce bulk behavior.

### 3.2.1 Slab Vacuum Thickness Convergence

CP2K allows for the printing of electrostatic potential and electric field information in the form of cube files. These could be used to analyze the potential (or electric field). The electric field is related to the electrostatic potential as follows:

$$\vec{E} = -\vec{\nabla}.V \quad (3.1)$$

Provided the vacuum thickness is sufficient, the potential is expected to be flat towards the boundaries in the  $a_3$  direction. Since the electric field is the gradient of the potential, a flat potential entails the absence of an electric field and there will be no coulomb interactions between periodic copies. A 2x2x5 slab is setup for both silver and gold, and a vacuum of 10Å on either direction is applied to the cell. 10Å is typically sufficient for neutral metals and is commonly used [42]. An 8x8x1 k-point mesh, cutoff of 300 Ry, relcutoff of 40 Ry and the TZVP basis set are used. An 8x8x1 mesh is used as the supercell is almost twice the size of the conventional bulk unit cells laterally. Figure 3.7 shows 5 troughs, corresponding to

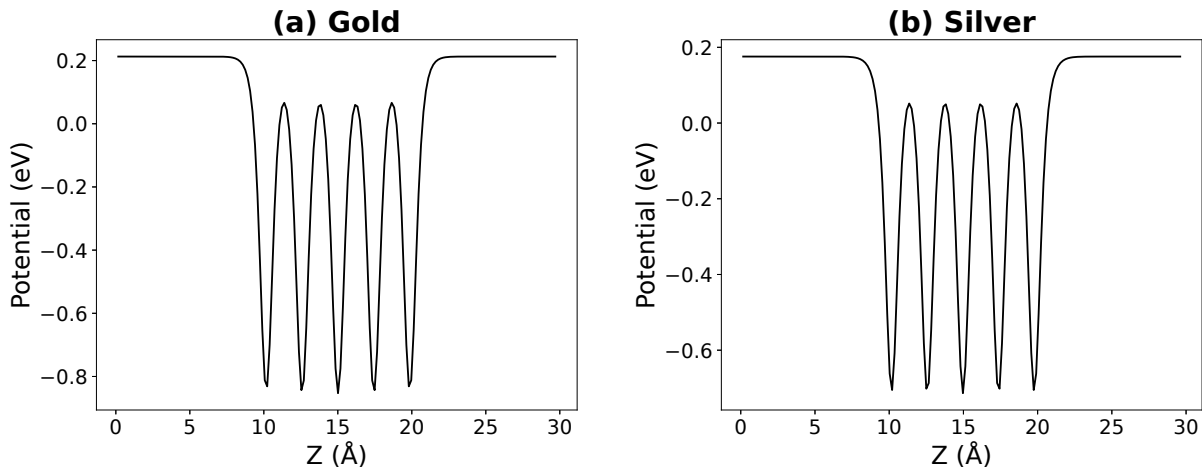


**Figure 3.7:** Vacuum thickness convergence for (a) gold and (b) silver 2x2x5 slabs

the number of layers and clearly shows flat-line potentials on either end of slabs as was expected. This indicates 10Å is more than sufficient for these neutral metals. Next, convergence tests are conducted, prior to finding the optimal slab thickness.

### 3.2.2 Convergence Tests

Cutoff tests were repeated for both gold and silver. For the former, it was seen in Figure 3.2 that gold is better behaved with respect to cutoff therefore, the cutoff was varied from 150 - 550 Ry similar to the bulk case. For silver however, the maximum cutoff was extended to 800 Ry. Interesting observations can

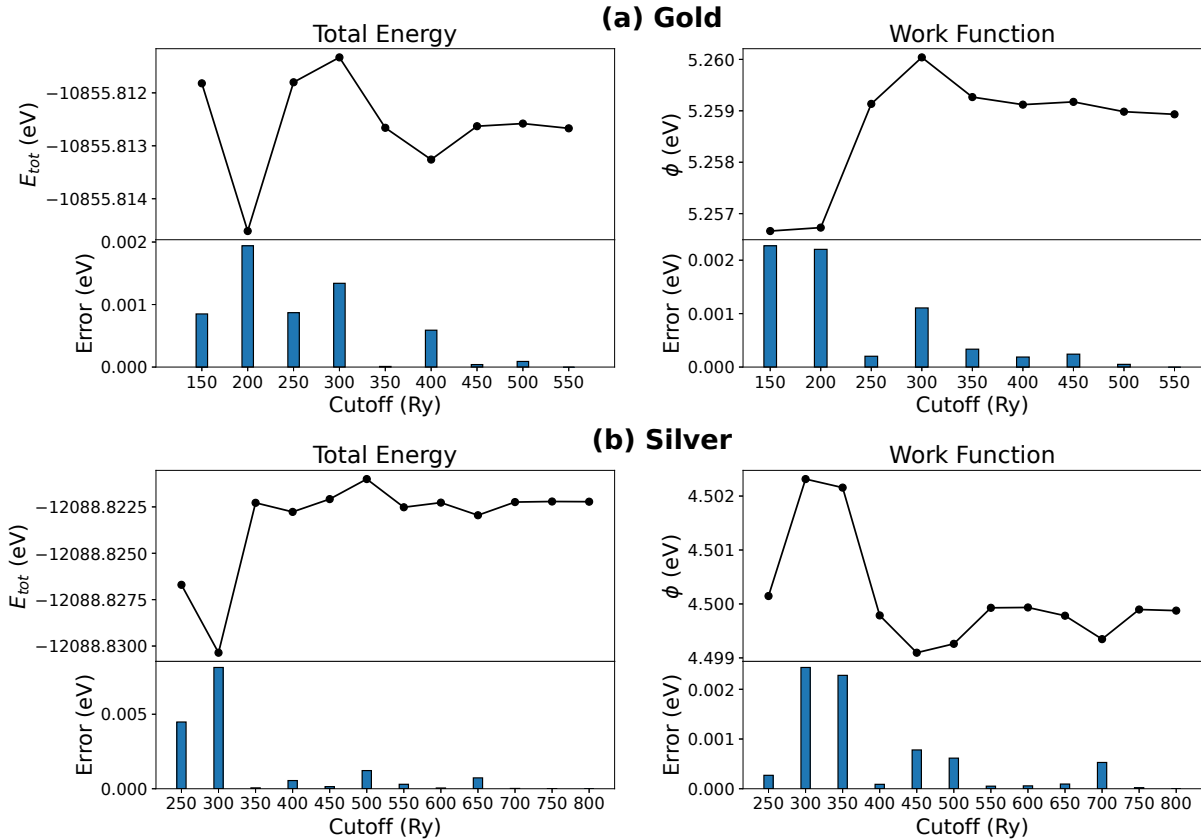
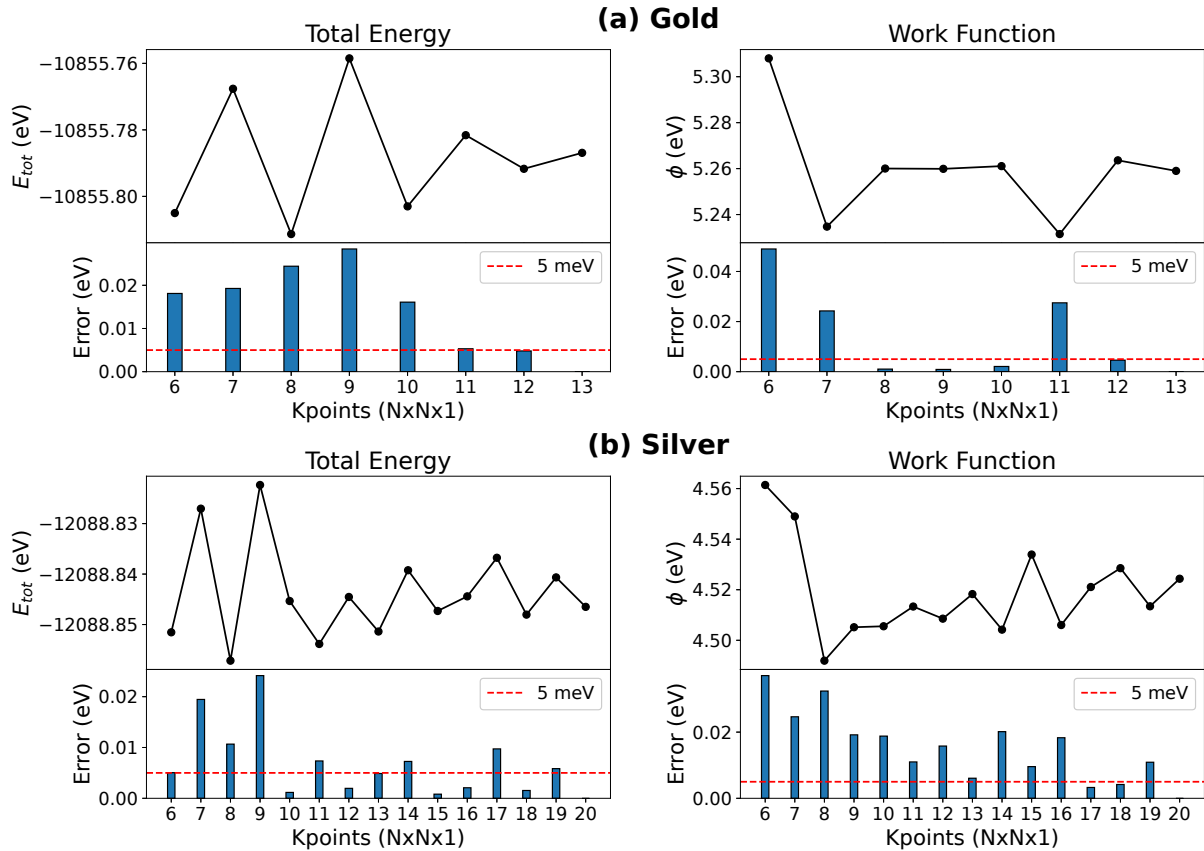


Figure 3.8: Variation of slab total energy and work function against cutoff for (a) gold and (b) silver

be made from Figure 3.8. A cutoff of 300 Ry is still sufficient for gold in terms of the total energy, but the error is now larger as expected. 350 Ry results in a much lower error in  $E_{tot}$  and  $\Phi$  and can thus be adopted for gold. For silver, the case is slightly different. 300 Ry now results in an error in  $E_{tot}$  that is greater than 5 meV. Similar to gold, a cutoff of 350 Ry is superior at minimal computational expense. The k-points ( $k \times k \times 1$ ) were varied from 6 - 13 for gold and 6 - 20 for silver. Both even and odd number k-points were used which is expected to lead to oscillations since the odd-number k-point mesh will not be gamma-centered in contrast to even-numbered k-points (making the latter favorable/efficient). Figure 3.9 shows oscillations in total energy and work function for both, which die out earlier for gold compared to silver. It can be seen in both cases that k-points as high as  $12 \times 12 \times 1$  are needed to meet the 5 meV error threshold for  $E_{tot}$ . As for  $\Phi$ , high k-points are needed for silver to get errors below 5 meV. It is thus sufficient to use  $12 \times 12 \times 1$  for both silver and gold, accepting the error in  $\Phi$  for silver. In the interest of probing the relationship between k-points and both  $E_{tot}$  and  $\Phi$  further, additional tests were run exploring an even wider range of k-points up to  $31 \times 31 \times 1$  and using only odd-numbered permutations to ensure similar centering schemes (to suppress oscillations). These tests involved runs using both 3-layer and 5-layer slabs to also investigate the size of the slab on the behaviour. The results can be found in the appendix A as Figure A.1. In short, Figure A.1 shows there is an important sensitivity in  $E_{tot}$  and  $\Phi$  values for silver towards k-points and that care should be taken if sufficiently high k-point values are not used.



**Figure 3.9:** Variation of slab total energy and work function against k-points for (a) gold and (b) silver

### 3.2.3 Slab Layer Thickness Convergence

The aim of this section of the work is to determine the right number of layers to use for the junction electrodes. The previous subsections involved establishing parameters to conduct this test that is referred to as slab thickness convergence. The word convergence hints at the framework by which the optimal electrode thickness is determined: the number of layers that converge  $\sigma$  and  $\Phi$  need to be determined. Convergence of these two parameters means that opposite surfaces are decoupled and the middle layers are in 'bulk' conditions since adding additional layers imparts no energy penalties ( $\sigma = \text{constant}$ ) or influence on ionization ( $\Phi = \text{constant}$ ). A series of calculations are run using slabs of size  $2 \times 2 \times N$ , where  $N$  is the number of layers and is varied from 3-16. Some metal slabs have been shown to converge over this range, whereas semiconductors require larger  $N$  values [20, 42]. The absolute middle layer is fixed for odd-layered slabs whereas the inner-two layers are fixed for even-layered slabs. To minimize differences in the numerical implementation (e.g. cutoff), a constant unit cell size is used for all 14 systems in which the  $a_3$  unit cell vector is set equals to the size of the cell of 16-layer slab + 10 Å vacuum (the largest cell).  $\sigma$  is calculated following the method of Fiorentini and Methfessel [42], with  $E_{\text{bulk}}$  being calculated as the difference in total energy of the 16th and 15th layer slabs ( $E_{\text{bulk}} = E_{16} - E_{15}$ ). Many observations can be made from Figure 3.10. It is important to mention that the calculation is repeated for a cutoff of 500 Ry. This was done in attempts to get  $\sigma$  and  $\Phi$  to convergence. Interestingly, there is little difference when the cutoff is increased for gold. There are some oscillations in the work function at higher layers (9-13). Overall, it can be said that the convergence is nearly reached for both silver and gold, with slight divergence of  $\Phi$  at 16 layers.

To use 16 layers (eight for each electrode) for the junction would be computationally expensive. Instead, a lower number of layers is desirable with close values of  $\sigma$  and  $\Phi$  but is nonetheless computationally cheap. Five or seven layer slabs are potential candidates which can be further investigated by plotting the PDOS of the middle layer in both cases and comparing with bulk PDOS (11x11x11 primitive unit cell) using a cutoff of 500 Ry, relcutoff of 40 Ry and a larger supercell (PDOS are not implemented for k-point). 8x8x5 and 8x8x7 slabs are investigated. The normalized PDOS of the 5 and 7 (Figure 3.11)

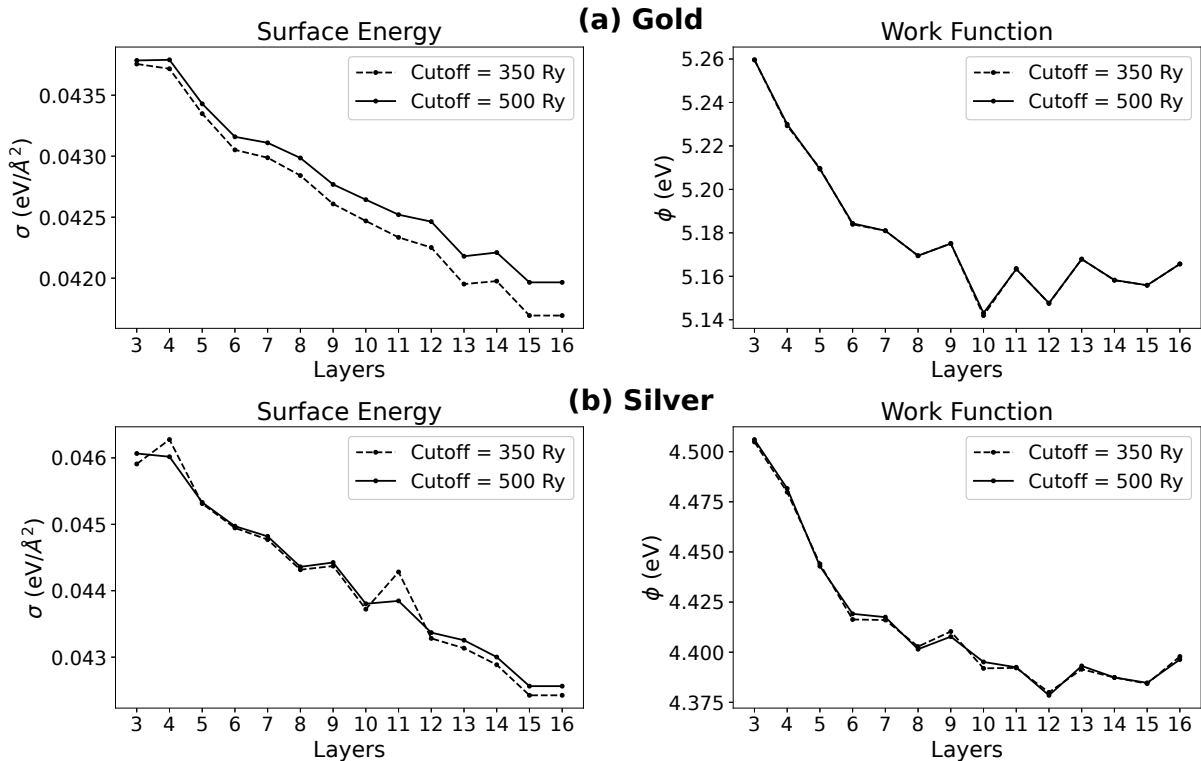


**Figure 3.10:** Surface energies and work function against number of layers for (a) gold and (b) silver

layer slabs for both metals closely follow the bulk PDOS. It can be seen that the PDOS of the 5 layer slab is not far off in both cases. Comparing values for  $\sigma$  and  $\Phi$  for the 5-layer slab with those from other DFT simulations and experiments, can further consolidate the choice. The uncertainty in the results in Table

**Table 3.3:** Optimized values of  $\alpha$  and  $\beta_0$  of Au and Ag compared to other sources

Source	$\sigma \left( \frac{eV}{\text{\AA}^2} \right)$		$\Phi(eV)$		
	GGA-simulations	Results	Exp.	GGA-simulations	Results
Au	0.0462, 0.0468 [60]	$0.0434 \pm 0.0015$	$5.33 \pm 0.06$ [61]	5.12, 5.15 [60]	$5.21 \pm 0.053$
Ag	0.0487 [60]	$0.0453 \pm 0.0028$	$4.53 \pm 0.07$ [61]	4.49 [60]	$4.44 \pm 0.058$

3.3 is determined from the values of the 16-layer slab. The values of  $\sigma$  and  $\Phi$  for 5 layer slabs agree with other GGA-PBE calculations. This selection is thus a good compromise for use in junctions and can be implemented by using 3 layers for the bottom electrode and two for the top. When PBC is applied, opposite electrodes stack to form 5 layers.

### 3.3 Gold Nanojunction

With the number of layers for the electrode established, three more steps are required to have a sensible junction model. Firstly, appropriate lateral dimensions for the junction electrodes need to be found. Suitability is based on two factors: electrodes must be large enough to isolate filaments (periodic wire copies should not interact) and accommodate ice-like (hexagonal) water layers on the surface. Secondly, the form of the filament, i.e. number of atoms and tip shape, also requires careful consideration. Thirdly, the highly abstract and ideal junction needs to be structurally and energetically optimized to a form that can be found in nature, in other words, a metastable state should be sought after since such structures are far from being globally stable (bulk gold is the most stable state). This section includes the results of the three aforementioned steps and ends with adding water to the final junction model.

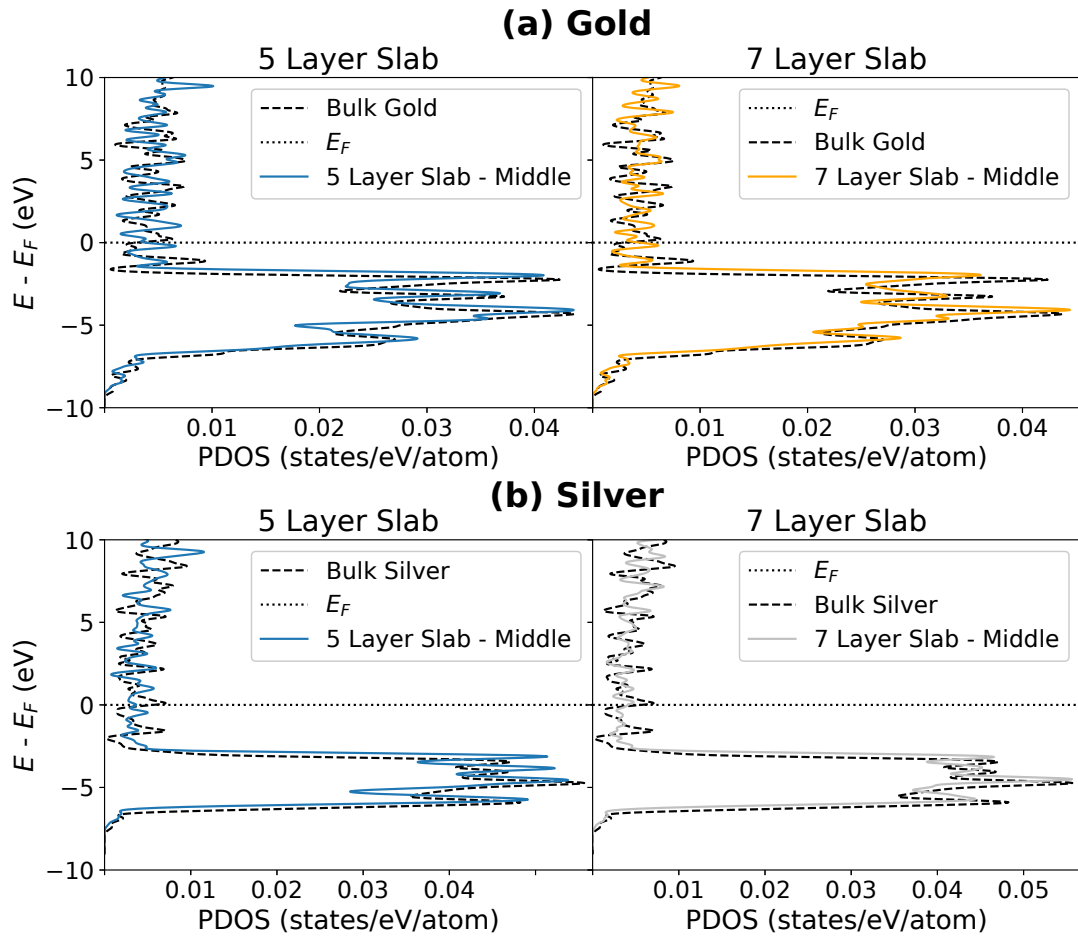


**Figure 3.11:** PDOS of the middle layers of 5-layer and 7-layer slabs for (a) gold and (b) silver

### 3.3.1 Lateral Size Optimization

For the purpose of defining appropriate lateral dimensions for electrodes ( $N_x, N_y, 5$ ), it suffices to use a 4-atom wire and the 3-atom base tip that was referred to in the previous chapter. Single point energy calculations are run for orthogonal unit cells where  $N_x = N_y = 4 \dots 12$  using even permutations only since  $N_x$  must be even for orthogonal FCC111 slabs for symmetry reasons. Using hexagonal cells would make solvation difficult later on and thus the focus is on orthogonal cells. The junctions can be built using ASE/Python by setting the initial interatomic spacing of atoms in the wire to the interplanar spacing and obeying the stacking symmetry of FCC111 surfaces for the electrodes+tips. Wire (or filament) isolation is bench-marked by introducing a variable, the wire formation energy:

$$E_{formation} = E_{junction} - (E_{electrodes} + E_{wire}) \quad (3.2)$$

Such a formulation (Equation 3.2) allows minimization of errors resulting from differences in the numerical schemes. However, a tricky parameter to equalize for the different junctions is the k-point grid density. From the previous section, it was found that  $12 \times 12 \times 1$  was sufficient for orthogonal  $2 \times 2 \times 1$  layers slabs. As the lateral size increases, the required k-point density decreases linearly. The  $8 \times 8 \times 5$  Junction would require  $3 \times 3 \times 1$  k-points however, odd-numbered k-points will not result in a gamma-centered grid. The  $10 \times 10 \times 5$  junction would also require an approximated k-point sampling.

Unsurprisingly, mismatches in k-point sampling seem to play a noticeable role in Figure 3.12.  $E_{formation}$  for the  $8 \times 8 \times 5$  and  $10 \times 10 \times 5$  are clear deviations. When the  $12 \times 12 \times 5$  junction is considered, it can be seen that changes in  $E_{formation}$  are minimal compared to the  $6 \times 6 \times 5$  junction. Since  $6 \times 6 \times 5$  electrodes can also accept hexagonal water layers,  $N_x = N_y = 6$  is sufficient for further calculations and will minimize the amount of water molecules needed later.

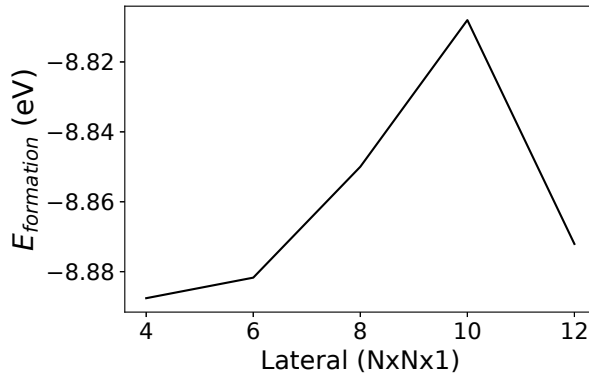


**Figure 3.12:** Formation energies of the gold junction for different lateral sizes

### 3.3.2 Structural Optimization

The decision on wire length (or number of atoms) can be mostly based on solvation. When modelling the solvated junction, it is necessary to have a junction that is big enough such that water experiences bulk condition (including its bulk density) in some region of the junction. The same is true for the lateral dimensions, which was explicitly discussed in the previous subsection. Otherwise, the notion of simulating water is invalid. To understand this, it is possible to visualize a mass density profile for a water layer between two electrodes. For systems of reasonable size and equilibrated water structures, as will be seen later, the mass density goes from increased values at the surface (DLs) to an almost flat line ( $1 \frac{\text{g}}{\text{cm}^3}$  for instance) in the middle. Therefore, care should be taken that the wire is long enough such that spacing between the two electrodes is sufficient. This spacing in turn, will differ when cell optimization is run for different wire sizes. Steps 2 (number of wires in atom) and 3 (structural optimization) can thus be probed together.

A start can be made with 4- and 5-atom wire junctions of size 6x6x5 which may satisfy the previous conditions related to water based on other computational studies. These junctions are initially highly ideal (unstable) and must be subjected to cell optimization (CELL-OPT). Compared to GEO-OPT, a stress is applied to the cell under CELL-OPT and the unit cell vectors, in addition to atomic positions, can be varied to minimize the total energy. In this study, the cell relaxation is restricted to the C-plane, as there is no physical reason to allow the AB planes to relax as well. It is expected for the wire interatomic spacing to respond to such optimizations as seen for free wires optimized in vacuum. The first layer of the bottom electrode can be fixed (corresponding to the middle of the 5-layers when PBC is applied). Using  $4 \times 4 \times 1$  k-points, 500 Ry Cutoff, 40 Ry Relcutoff and the TZVP basis set the following results were obtained:

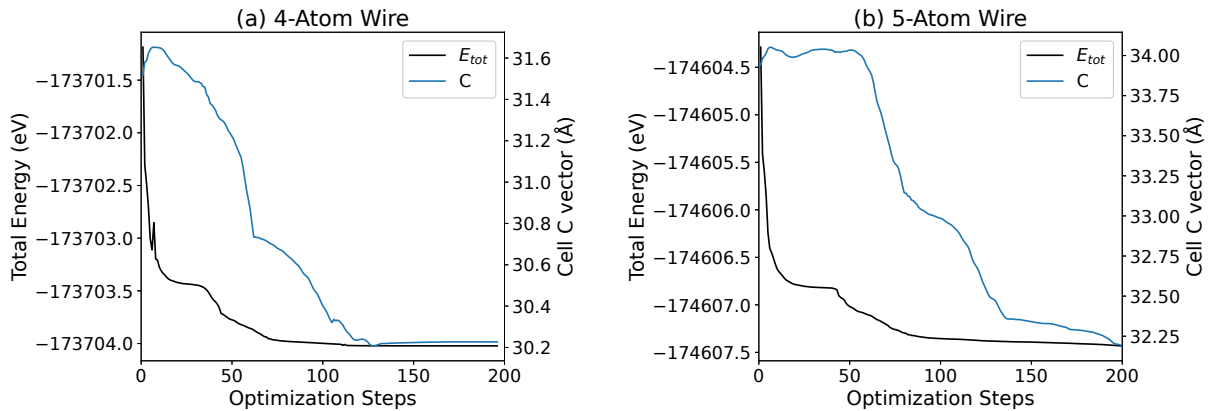


**Figure 3.13:** Variation of energy and the cell  $a_3$  vector during cell optimization for two junctions with differently sized wires (a) 4-atoms and (b) 5-atoms

Figure 3.13 tracks both  $E_{\text{tot}}$  and the size of  $a_3$  for both junctions against the number of optimization iterations. Towards the end of the CELL-OPT, both  $E_{\text{tot}}$  and  $a_3$  flat out for the 4-atom junction, indicating

the presence of a metastable state. The metastable label stems from the expectance of contraction (and energy minimization) to proceed, given a large number of iterations, until bulk gold formation.

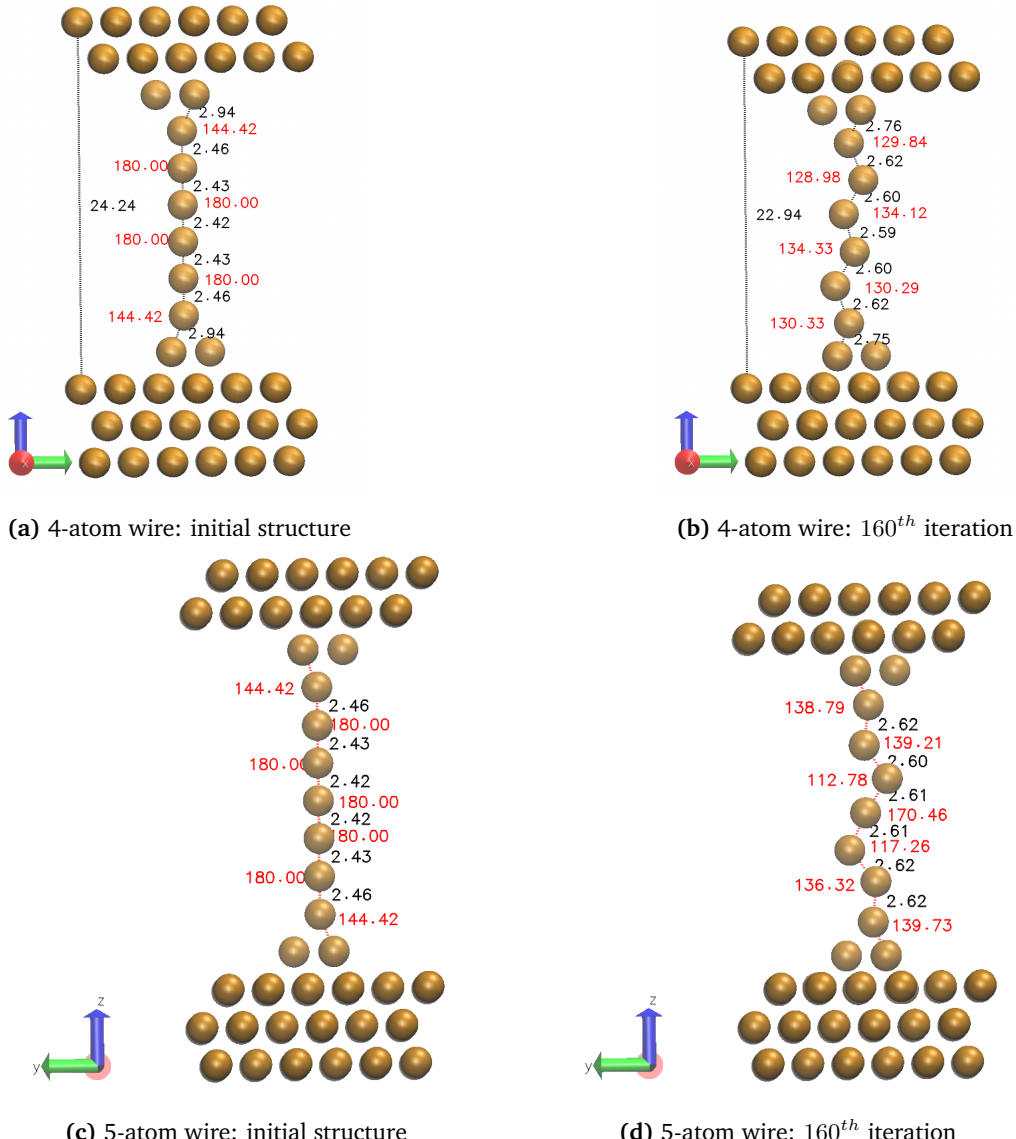


**Figure 3.14:** Structural evolution of the 4- and 5-atom wire gold junctions. Bond lengths and angles are labelled in black and red respectively.

Figure 3.14 provides visuals of CELL-OPT process. It can be seen in both cases, that the junctions contract and the wires take on zigzag forms. In both the 4 and 5 atom wires the average interatomic spacing is around 2.62 Å, which has also been observed for free wires optimized in vacuums [62, 63]. The angles are around 130° for the 4-atom wire which is an almost perfect zigzag, while the more asymmetric 5-atom wire has a range of angles. The observed meta-stability of the 4-atom wire both structurally and energetically make it satisfactory for use in the next simulation steps, as a sensible approximation of a device that may be found in nature.

### 3.3.3 Solvation

With the final junction form established, the next step is to add water or solvate the junction. There are different ways to approach this task which include using software packages to directly solvate the junction as is done for proteins for example, assigning water molecules corresponding to a set density at a specific temperature. However, most packages solvate the whole system and do not have the flexibility to solvate around a wire between two electrodes. Instead, what is done here is to calculate to the best

extent possible, the exact volume available for water and calculate the corresponding number of water molecules that give a density of  $1\frac{g}{cm^3}$ , which is an approximate value of the density of water at room temperature and pressure.

The exact volume available to water can be thought of as the exposed space encompassed by the two electrodes and the wire. To get this volume, a cuboid could be drawn with  $x$  and  $y$  dimensions equal to the  $a_1$  and  $a_2$  vectors and the  $z$ -dimension beginning from the horizontal line crossing the average of the center of atoms at the surface layer of the bottom electrode and ending at a similar horizontal line crossing the center of atoms at the surface layer of the top electrode. The exposed volume available is then, the volume remaining after the half spheres from both surfaces, the 12 atom-filament, and the voids formed between atoms resting on three other atoms (such as tip atoms immediately on the base) are subtracted. For the latter, there are 8 such instances, the two atoms on tips and 2x3 tip atoms on electrode surfaces which seal voids. In mathematical form:

$$V_{exposed} = V_{box} - \left[ 2 \left( 36 \times \frac{2}{3} \pi R^3 \right) + 8V_{void} + 12 \left( \frac{4}{3} \pi R^3 \right) \right] \quad (3.3)$$

The radii can be calculated using  $R = \frac{\alpha}{(2\sqrt{2})}$ . The calculation of the void volume consists of two parts, firstly the equation of the volume of a tetrahedron can be used to obtain the volume between 4 vertices (atomic centers) A, B, C, D with coordinates  $i$ :

$$V_{tetrahedron} = \frac{1}{6} \times \vec{AD} \cdot (\vec{AB} \times \vec{AC}) \quad (3.4)$$

Secondly, the volume of the parts of the atoms within this tetrahedron, which in mathematics are called spherical triangles, need to be determined:

$$V_{sphericaltriangle} = V_{sphere} \frac{S_{ABC}}{S_{sphere}} \quad (3.5)$$

The surface area of the spherical triangle  $S_{ABC} = R^2 E$  where  $R$  is the atomic radius and a  $E$  is the spherical excess which can be obtained using L'Huilier's Theorem [64]. Assuming the portion of the spherical triangle is regular with all angles equal to  $60^\circ$ , the excess,  $E$ , can be obtained via:

$$E = 4 \arctan \left[ \left( \tan \frac{\pi}{12} \right)^{3/2} \right] \quad (3.6)$$

Finally, for each void:  $V_{void} = V_{tetrahedron} - V_{sphericaltriangle}$ . The results of these calculations are summarized in Table 3.4. The number of water molecules can be obtained simply by  $N_{water} = \frac{\rho V_{exposed} N_A}{M_R}$ . From

**Table 3.4:** Results of volume calculations of the empty space available for water

Parameter	$V_{box}$		surface hemispheres	filament	$V_{void}$		$V_{exposed}$
Volume ( $\text{\AA}^3$ )	5633.10	-	493.21	164.40	6.34	=	4969.15

this,  $N_{water} = 166.2 \approx 166$  molecules. Using this information, Packmol [65] can be used to generate a water box with 166 molecules arranged in a way that leaves a cylindrical void (to avoid clashing with wire atoms). The box is generated in a compressed form, such that there are spaces between the periodic copies of the water boxes. Failure to do so would lead to errors when classical MD is run. Packmol generates a random water structure. Moreover, although careful calculations were used to determine the appropriate number of water molecules, it is not confirmed that we have the correct water density. For these two parts, classical MD was run in CP2K, first to obtain an equilibrated and improved water structure and to ensure the density is correct.

## 3.4 Classical Molecular Dynamics

Two main aspects are of interest in this section namely, the water structure (including the DL) and the density. Obtaining a proper structure can appreciably reduce computational time needed for equilibration in AIMD. Getting the density right is critical as it is an indicator of the phase and conditions of water being modelled. For the structure, classical MD following the NVT ensemble can be run. As a reference, a system will also be run taking excluding the filament in which the available volume introduced will be accounted for and extra water molecules added.

### 3.4.1 NVT Equilibration

As mentioned in Section 2.3.2, TIP3P water with LJ potentials for Au-H and Au-O were selected as forcefields. The gold atoms are collectively fixed at their positions from vacuum relaxations, allowing water to rearrange. Temperature was set to 300K while the CSVR thermostat TIMECON was set to 1000 fs. Over 30 ns of MD time was achieved in a span of few days. No special equilibration scheme was followed since gold is fixed and will not be structurally affected. Kinetic energy and conserved quantity (CQ) results from the last 15 ns can be seen below: The system can be said to be well equilibrated during

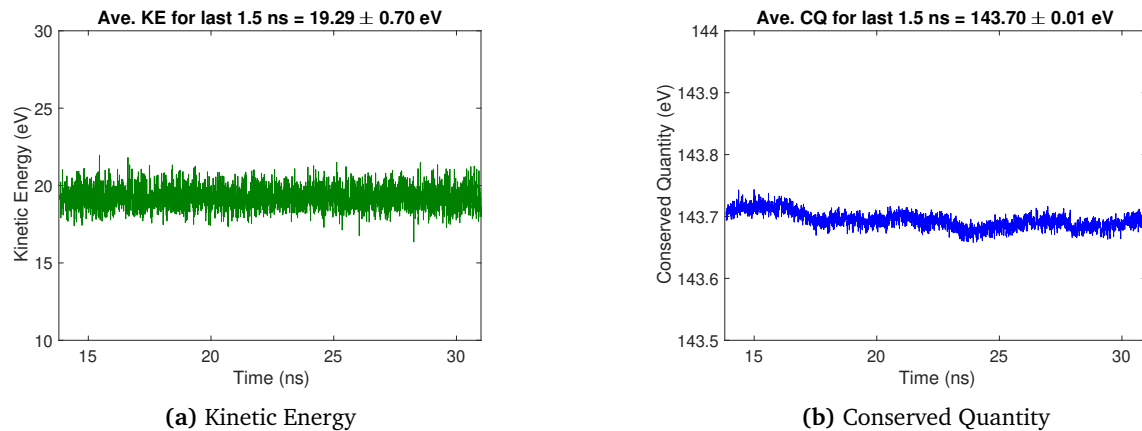


**Figure 3.15:** K.E and CQ profiles for the last 15 ns of the classical NVT run

this time period based on Figure 3.15. Variations/oscillations of variables such as temperature are natural in MD simulations. Particular attention should be given to the conserved quantity (CQ), whose change can be considered as a measure of numerical accuracy. Therefore, the convergence of CQ validates the MD setup. The average mass density can also be investigated using a [custom MATLAB code](#). The code partitions the axis of choice into bins of desired number/size (which extend to cover other axes) and the number of water molecules in each bin is counted providing a picture similar to a histogram. The mass density can then be calculated across the bins for each snapshot in the trajectory file before finally obtaining an average density. In the case of this simulation, snapshots are taken every 5ps and the last 15 ns are analysed meaning it is reasonable to assume that in any analysis concerning the trajectory file, a wide range of distinct configurations or states will be sampled.

There are some aspects to consider regarding plotting mass density profiles. Firstly, it is necessary to determine which axis to partition. Here, both the z- and x-axes will be partitioned. The former should be sampled to investigate whether or not water approaches bulk conditions in the middle of the junction. The latter can be used to investigate whether bulk water conditions are observed on either end of the junction, which is expected for such a junction. A second aspect is the number of bins which governs the resolution of the mass density plot. For this, a start could be made using 10 bins/Å. This could be adjusted to attain the desired resolution. Thirdly, the size of the bins need to be specified. This is particularly important for the case where bins are sampled across the x-axis since, the bins should not extend to the metal electrodes.

Figure 3.16 shows the mass density across the z-axis. There are two sets of peaks separated by a relatively flat line in the middle. These peaks correspond to water layers on either surface. The larger peaks represent the highly dense, first layer structured on the surfaces. The second, less intense peaks correspond to the second layer of the DL and are less intense compared to the first as the metal-water interaction strength fades with distance. A dink can be seen at 15Å and the mass density does not approach a flat-line in the middle. This may be attributed to water layers surrounding the wire. Overall the average density is quite close to  $1000 \frac{kg}{m^3}$ , and the true value is even closer since the volume of the filament is not excluded from relevant bins. To determine the size of the bins for sampling across the x-axis, the tails of the second peak from Figure 3.16 can be used to exclude both the electrodes and the first two water layers. The latter are excluded to observe bulk conditions on either end of the x-axis (if present).

It can clearly be seen in Figure 3.17 that there are pockets of bulk water on either end of the junction as expected. These are in the form of nearly flat lines close to  $1000 \frac{kg}{m^3}$  in the first and final few angstroms.

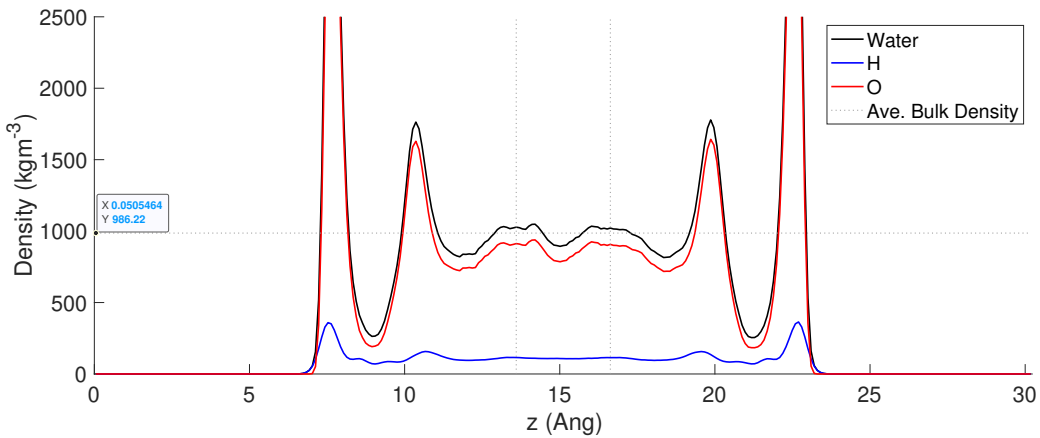


**Figure 3.16:** Mass density profile along the z–axis using data from the 15 nanoseconds of the classical NVT run

The position of the wire is superimposed onto the image. The small peaks can be thought of as the outer water layers surrounding the wire, whereas the larger peaks correspond to the surface layers. The drop in density in the middle obviously results from the presence of the wire. It should be noted that the density profile is not perfectly symmetric (when considering either end of the wire). This is possibly due to the wire not being located in the middle of the junction. One of the main parameters for analysing water

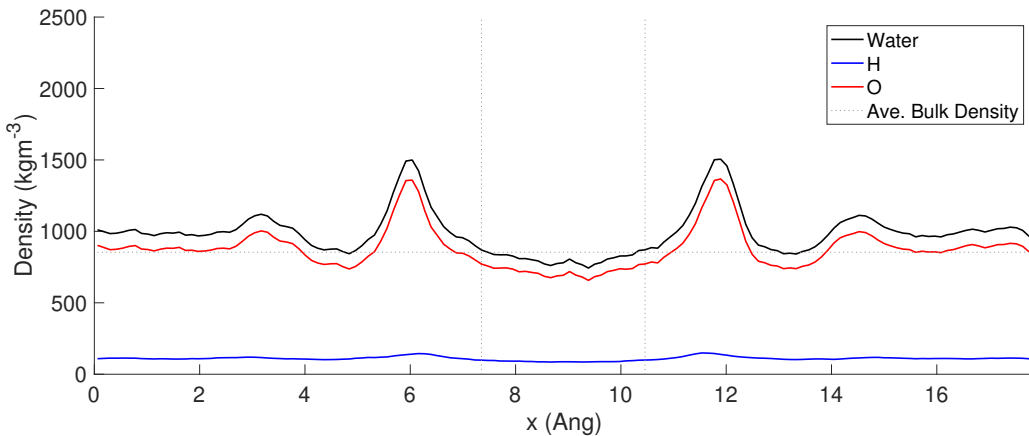


**Figure 3.17:** Mass density profile along the x–axis using data from the 15 nanoseconds of the classical NVT run

MD results is the radial distribution function (RDF). The RDF provides the probability of finding a set of particles as a function of the radial distance from the center of a reference particle [66]:

$$g_{\alpha\beta}(r) = \lim_{dr \rightarrow 0} \frac{\rho(r, dr)}{4\pi(N_{\alpha\beta}/V)r^2 dr} \quad (3.7)$$

$\rho(r, dr)$  is the number of atom within the infinitesimal shell spanned by  $r$  or  $r + dr$  and is averaged over all trajectory frames.  $N_{\alpha\beta}$  is the number of pairs of the two atoms or species considered,  $V$  is the system volume and  $r$  is the distance between the pairs of atoms.  $\rho(r, dr)$  is normalized such that any deviation from the value of  $g_{\alpha\beta}(r)$  from unity can be interpreted as structuring or correlation in the system [66].

The resulting RDFs of different models including *ab initio* models have been compared extensively in the literature. Figure 3.18 shows  $g_{OO}(r)$  and  $g_{OH}(r)$ . Beginning with the former, a peak can be seen at around 2.7–2.9 Å, in agreement with experiments and other TIP3P simulations, which corresponds to the first coordination shell [67, 68]. Water does not have long-range order akin to crystals. However, there are definitive structures relative to the center of atoms resulting from electrostatic interactions and their defined sizes. Here, the height of the peak is larger than other models (including TIP3P results) and

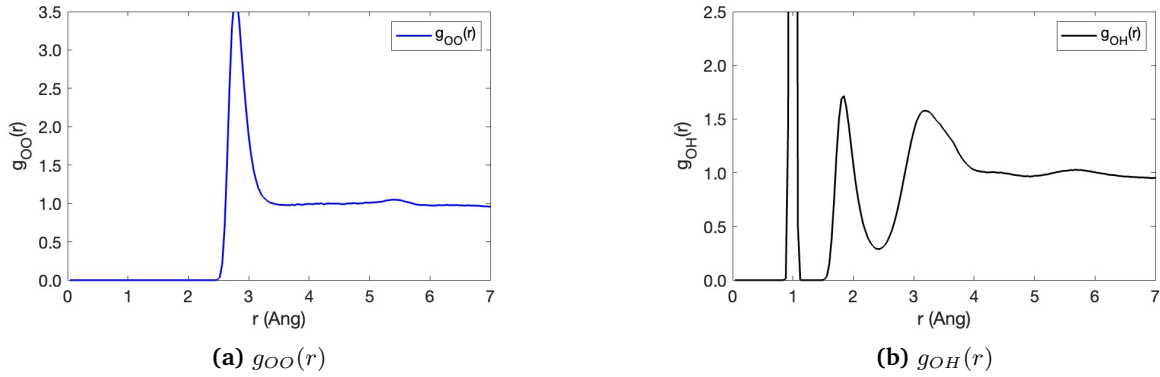


**Figure 3.18:** RDF of (a)O-O and (b)O-H from last 15ns of the classical NVT run

experiments , where it is typically between 2.5-3.0Å representing a slight 'over-structuring' at the first coordination shell [68]. It is unclear whether the presence of gold atoms plays a role in this observation. It has been suggested that the  $r^{-12}$  in the LJ of the TIPnP is too repulsive and may lead to overstructuring in the first shell of the O-O RDF [66]. The interplay of water-water and metal-water interactions may augment this. For other force-fields and in experiments, 2nd and 3rd peaks with decreased heights are observed for the  $g_{OO}(r)$ , in contrast to Figure 3.18 where the second peak (around 4.5Å is completely missing. This is commonly the case for TIP3P models, which show significant 'under-structuring' beyond the first coordination shell. More advanced models in the form of TIP4P and TIP5P water have been developed to correct this.

For  $g_{OH}(r)$  on the other hand, there is an initial, large peak which stems from O-H bonds of individual water molecules. The second and third are related to neighbouring water molecules. The position of the second peak (around 1.8-1.9Å) is in close agreement with experiments (and other simulations) however the height is slightly higher compared to experiments and other TIP3P simulations, similar to  $g_{OO}(r)$  [67, 68]. The position (~ 3.2Å and height (~1.6) of the second peak closely agree with experiments (3.3Å 1.6) and other TIP3P simulations (3.24Å 1.44) [68]. In general, the RDFs show that the resulting structure is reasonable.

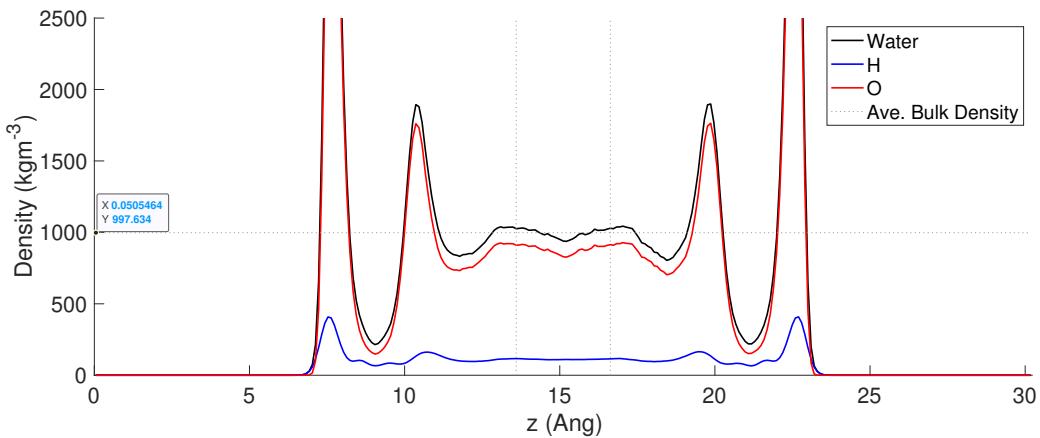


**Figure 3.19:** Mass density profile for a classical NVT run of a junction with the wire excluded

To get a better sense of the results, the same simulation was repeated for a junction with no wire. Figure 3.19 shows the density profile along  $z$ . It can be noticed that the dip in the middle of the junction is significantly reduced compared to Figure 3.16. It can be concluded that the dip results mostly from the presence of the wire and not a small cell size. The profiles are similar otherwise, with the characteristic surface peaks. The average density is closer to  $1000 \frac{kg}{m^3}$ . Since there is no error associated with excluding the wire from the bin volumes, these plots show that the method employed earlier for density is correct. The RDF results for the system with no filament differ very little if anything from the case presented above and are not included here. This means that any contributions from the metal-water interactions

are possibly dwarfed by surface-water interactions.

### 3.4.2 NPT Run

With a reasonable structure obtained, the matter of liquid density remains partially complete. In general, when modelling liquids using MD it is common to run simulations following the NPT ensemble. Ensuring a constant pressure of 1 atm means the cell will readjust leading to a water density of  $1 \frac{g}{cm^3}$ . An attempt was made to run with NPT following the NVT run. The unit cell was constrained to variations only in the  $C$  plane (or  $a_3$  vector) as done with CELL-OPT. Since the gold atoms must now be dynamic in contrast to the NVT run, a force-field for gold needs to be specified. For this, the EAM model is used as was described in the previous chapter. Despite care in the initialization of temperature, extreme stress/pressure variations led to a rupture of the wire and massive oscillations in the physical separation between the two electrodes. It was concluded that water's low compressibility coupled with the relatively small system size naturally induce such large pressure (and thus density) variations. Any such variation in pressure may rupture the wire which will not form again. An attempt was also made to investigate this further by running QM/MM on CP2K where water was treated classically and gold quantum mechanically. This was done to see if the metallic bonds introduced by DFT may dampen any structural changes from pressure variations. The computational cost however was relatively high using this method. Considering the mass density results from the previous section, it is not unreasonable to assume that the water density here is correct since it was measured in different ways. Consequently, it may not be necessary to run NPT using QM/MM and AIMD can be commenced instead.

## 3.5 Ab initio Molecular Dynamics

The previous sections covered were mostly related to setting up the system and preparing for AIMD. It can be recalled that, the main objectives of this study are to study the metal/water interface in such a novel structure and observe the dynamics of wire in a solvent, which might reveal alterations in properties such as conductance. After obtaining a good guess configuration for water, AIMD can be run. As gold is now dynamic, it is necessary to equilibrate the system without imparting severe structural deformations. After that, there will be a production run which entails collection of data to be used for analysis. The analysis consists of two parts. Firstly the structure of water (e.g. mass density) and the nanojunction (wire) will be reported. The latter is expected to be influenced by the solvent. Secondly, electronic structures, particularly the projected density of states (PDOS) will be investigated.

### 3.5.1 Equilibration

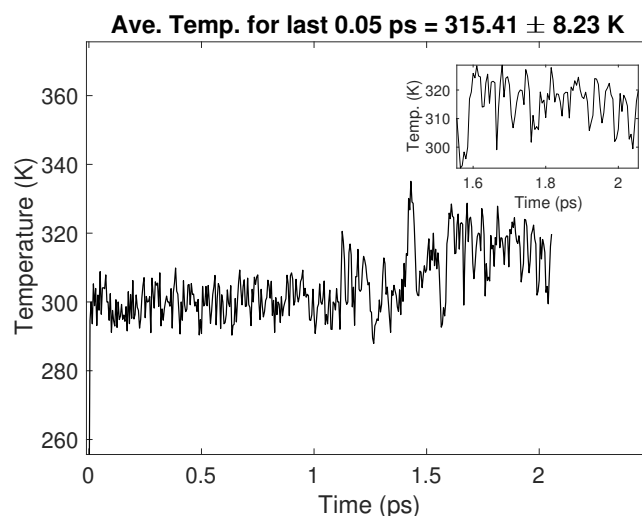


**Figure 3.20:** First 2ps of AIMD NVT run with heavy thermostat settings for temperature control

In the classical NVT run, the system was initiated and run with constant settings for the total 30 ns of MD time. This intentional move saw an explosion in temperature in the first few ps which results from the fact that the system experiences tremendous forces initially. These forces arise from the artificial, compressed initial configuration. The major jump in temperature is not necessarily negative as it may allow exploration of water configurations on the PES that may not be accessible otherwise. However, following the same strategy here would be costly since the junction would lose its structural integrity. Instead, the TEMPTOL and TIMECON keywords need to be adjusted to heavily act on the temperature and prevent it from rising exceedingly. TEMPTOL and TIMECON are both settings that trigger the thermostat. The prior triggers the thermostat if the set temperature is exceeded by a certain amount (e.g. 10K) and the latter triggers the thermostat periodically. Such heavy 'thermostating' affects dynamics meaning, it needs to be applied only for the first few ps until temperature is steady.

Figure 3.20 show the evolution of temperature in the first 2ns, with the energy every printed 10 MD steps (5fs). Until around 1.3ps, TEMPTOL was set at 10K whereas the TIMECON was set at 100fs. There is clearly heavy 'thermostating' as the temperature is very well controlled. After 1.3ps TIMECON was set at the standard 1000fs whereas TEMPTOL was raised to 40K precautionarily. This is reflected in Figure 3.20 as the temperature oscillations become larger. However, TEMPTOL does not appear to be activated and harsher thermostat settings were not re-imposed. Structurally, the wire maintains structural integrity in this stage without major changes but appears diffuse unsurprisingly.

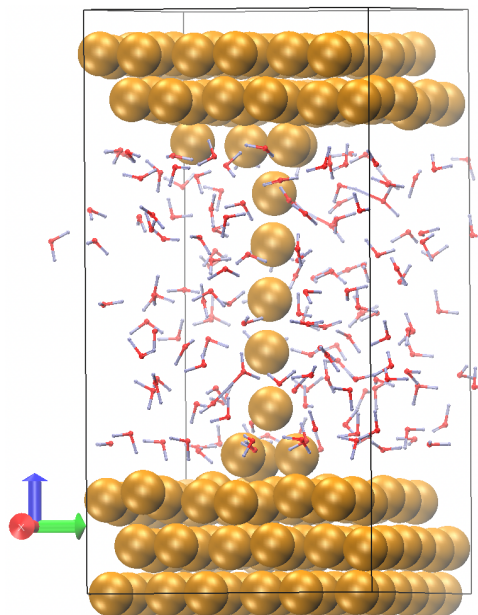


**Figure 3.21:** Structural form of the wire after 4.652ps of AIMD showing a major transformation

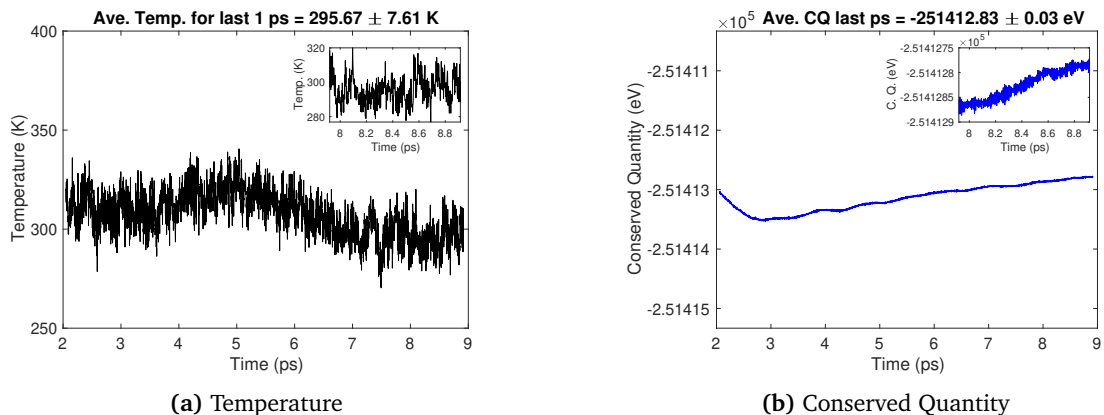


**Figure 3.22:** Temperature and CQ profiles for the last picoseconds of the AIMD run

The AIMD was run for several more picoseconds (as long as the project allowed) and TEMPTOL was deactivated at around  $4.5\text{ps}$  after confirming the temperature does not exceed 340K. A major structural change was observed from around  $3 - 5\text{ ns}$  which saw the wire stretch and expand from a zigzag shape, pushing the upper tip atom into the tip and replacing one of the original atoms in the upper base. The now formed structure, shown in Figure 3.21, showed greater stability. The structural change is also reflected in the energy and temperature profiles in Figure 3.22 where there is a noticeable change around that time period. The system begins to stabilize around this new structure from around  $5 - 7\text{ps}$ . The CQ observed in Figure 3.22 along with the temperature can be used as indicators of equilibration. Beyond the 8-picosecond mark, the system is energetically equilibrating and the structure sees no major changes. As these are nonequilibrium processes, it is not appropriate to rely on such minimal dynamics to make comments on stability of the structures. With the shortage of AIMD data, the results from  $6.5\text{ps}$  onwards, which still depict ongoing equilibration, can be counted as the production run and can be used for analysis.

### 3.5.2 Water Structure

During analysis of AIMD runs, it is necessary to obtain statistical averages using samples from the production run data. For the purpose of analyzing the water and wire structures, 25 trajectory samples are drawn from  $6.5 - 8.925$  (the last 2.425 picoseconds). This corresponds to sampling roughly ever 0.1 picoseconds. Beginning with the structure of water, the mass density and RDF shall be probed similar to the analysis of the classical MD run. The mass density profiles are plotted along both the  $x$ - and  $z$ -axes.

#### Mass Density

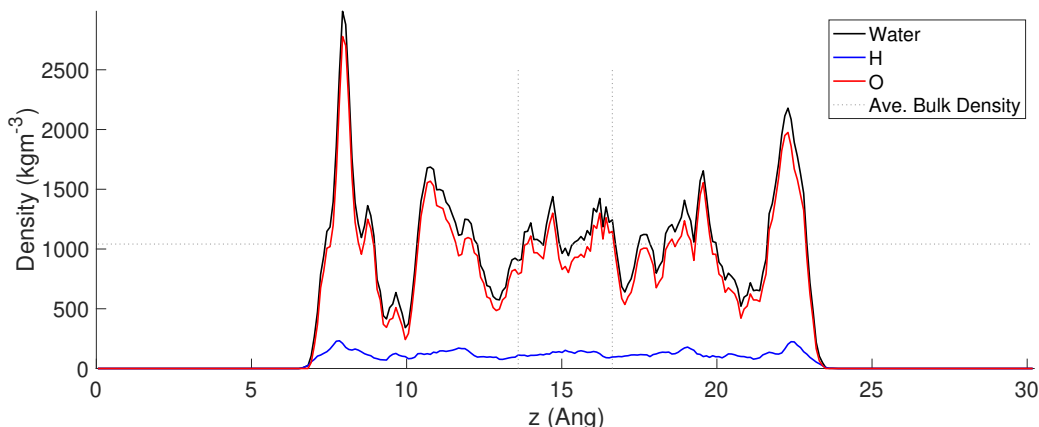


**Figure 3.23:** Mass density profile along the  $z$ -axis for the last 2.425 picoseconds of the AIMD run

Several important features are noticeable in Figure 3.23 including significant changes compared to the classical MD counterpart (Figure 3.16). There are now separations in the peaks with the molecules closest to the lower electrode appearing as barely visible shoulder peaks at around  $2.6\text{\AA}$  away from the electrode surface. Such molecules are typically O-down molecules with coordinate bonding with the metals. A large peak can be around  $3 - 3.1\text{\AA}$  corresponding to a major water layer. These two values are in agreement with a prominent AIMD study that employed the GGA-PBE functional to study the Au(111)/water interface [69]. The major peak in the aforementioned study however was closer to  $3.3\text{\AA}$ . There is a second shoulder on the right side of the large peak corresponding to another layer at around  $4\text{\AA}$  from the surface. The significance of this peak is unclear. The peak closest to the other electrode surface contains no shoulder peaks. Judging by the full mass density profile which shows several minor peaks, there is possibly insufficient statistical averaging. There is also less contrast in the mass density profile towards the middle of the junction, where there are still significant peaks. This has been observed in other studies and is possibly due to the weak  $\text{Au} - \text{H}_2\text{O}$  interactions that do not sufficiently perturb the hydrogen bond network under such time frames. Lastly, the major peaks closest to either surface are of different magnitude. This difference in peak height reflects the now asymmetric form of the junction, where there is an additional gold atom on the upper surface causing a lower density. The

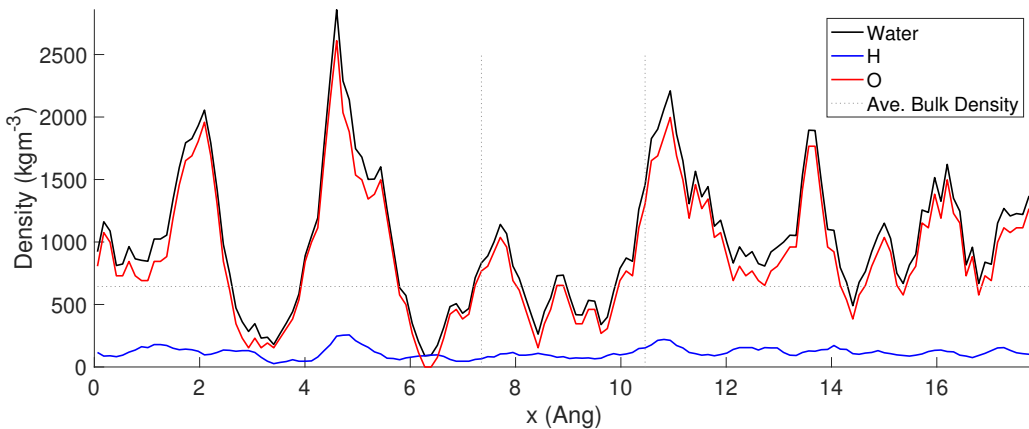


**Figure 3.24:** Mass density profile along the  $x$ -axis for the last 2.425 picoseconds of the AIMD run

density profile along the  $x$ -axis is also reported here (Figure 3.24). Large peaks can be observed at 4.7 $\text{\AA}$  and 10.8 $\text{\AA}$  which correspond to 2.8–3.1 $\text{\AA}$  away from the wire atoms on either direction. Shoulder peaks can also be seen closer to the wire similar to the mass density profile across  $Z$ . In the region where the wire/tips/bases ( $\approx 7 \pm 1.48\text{\AA}$ ) the density decreases as expected, with a peak relatively smaller peaks that are possibly due to structures around the wire and bases in the  $y$ -direction. The peak at around 4.7 $\text{\AA}$  is larger than that at 10.8 $\text{\AA}$  reflecting the asymmetry of the wire. Outside of the two large peaks, there are further peaks and structuring. Again here, there is a possible interplay between hydrogen bond networks and insufficient statistical averaging. The density profiles on either end of the junction are not continuous/similar which is expected for PBC calculations. This is an artefact from the post-processing tool used to generate the profiles along the  $x$ -direction. The bins do not partition the axis in a way that accounts for PBC. The previous two diagrams open up the question of whether there is ‘overstructuring’ in water. The RDF profiles act as indicators of the extent of structuring as discussed earlier.

### Radial Distribution Function

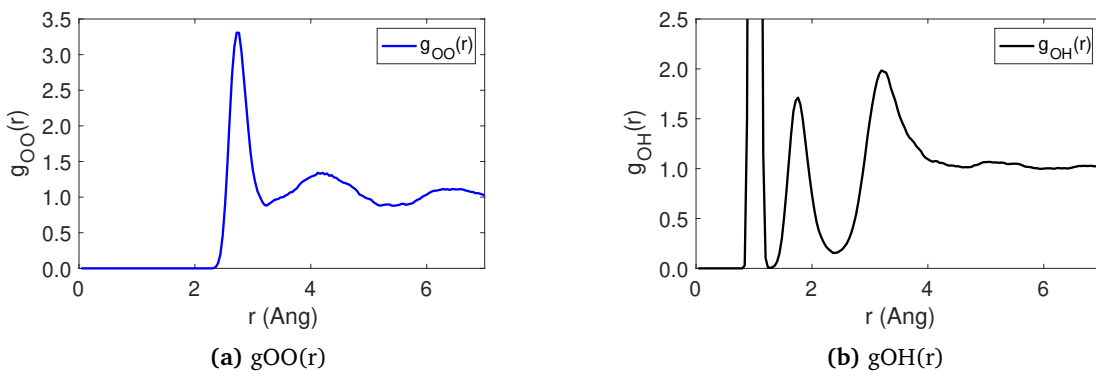


**Figure 3.25:** RDF of the (a) O–O and (b) O–H pairs for the last 2.425 picoseconds of the AIMD run

The RDFs of the O–O and O–H occurrences are reported above. It can be seen in Figure 3.25 that there are now three peaks in contrast to TIP3P results, in which water was ‘under structured’. A first peak is seen at (2.76 $\text{\AA}$ , 3.3), while the second occurs at (4.2 $\text{\AA}$ , 1.34) and the third at (6.44 $\text{\AA}$ , 1.11). These results are more closely aligned with experiments compared to the classical MD results as the second and third peaks are experimentally observed. The position of the peaks are slightly closer to the origin compared to experiments where for instance the first peak is located at 2.88 $\text{\AA}$  [68]. This is commonly seen for calculations employing the PBE functional [3]. The intensity of the peaks correlate better with experiments compared to standard PBE functional where they are appreciably overestimated [3]. Results so far do not indicate excessive structuring. The O–H RDF is quite similar quantitatively to that obtained from the Classical MD run. In general, there is an improvement of the structure relative to experiments

as is expected for the VDW-corrected PBE functional [3]. Therefore, water appears to be described adequately well.

### 3.5.3 Wire Structure

A very important aspect of the AIMD results is wire dynamics. The wire is expected to transform structurally when in the presence of water and at around 300K, starting from a structure optimized in vacuum at 0 K (CELL OPT). Significant changes and/or fluctuations in the shape and form can also result in changes in the electronic structure and conductivity. To characterize structural changes, the angles and separation between wire atoms are plotted as functions of the MD run time. Figure 3.26 contains 3 parts.

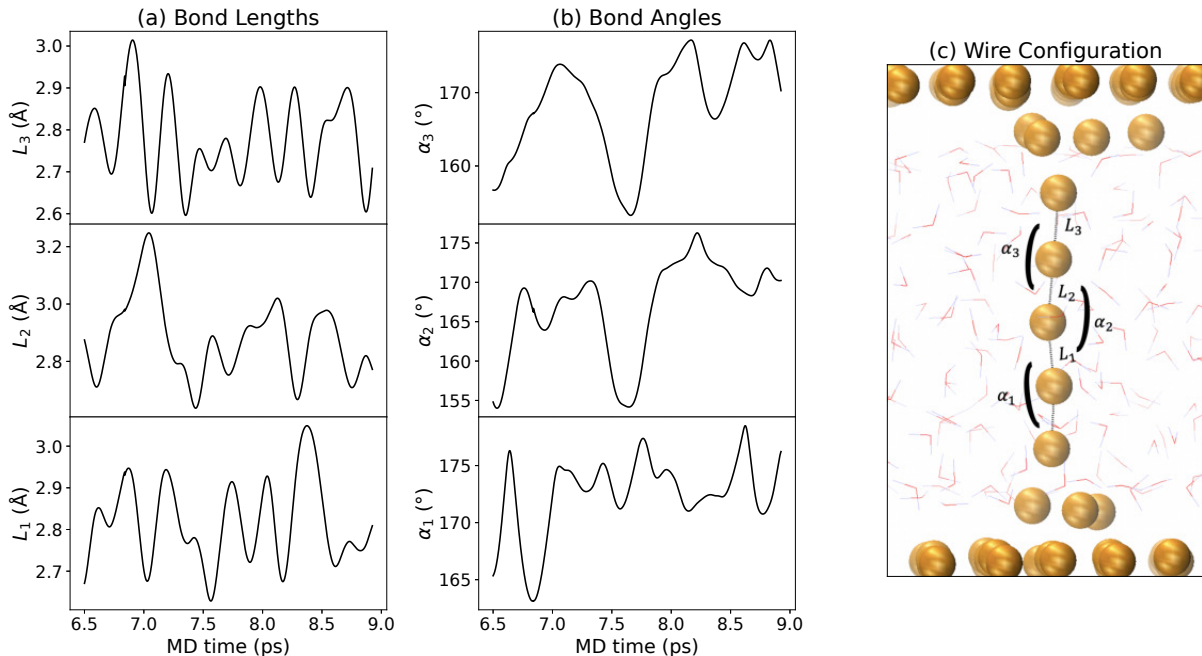


**Figure 3.26:** Variation of wire bond (a) lengths and (b) angles during the last 2.425 picoseconds of AIMD. (c) Shows the lengths and angles considered

The first two, (a) and (b), depict variations in interatomic separations and bond angles respectively. An image of the junction (c) is included that includes labels of the particular lengths and angles investigated. Three lengths and angles were chosen that are relevant to the wire structure. It can be immediately noticed in Figure 3.26(a) that variations in lengths are considerable, with the lengths remaining appreciably larger than 2.62Å found for vacuum. An increase in separation between the atoms is expected due to the increase in temperature. Thermal expansion coefficients indicate gold should expand by around 1–1.5% [70]. However, expansions are much greater here. It is interesting to see that around 7 picoseconds,  $L_2$  even exceeds 3.2Å. It is worth noting that early experimental work on synthesizing atomic gold wires by Ohnishi et al.[71] using electron beam lithography stirred computational research when they visualized using TEM a stable gold nanojunction of 4 atoms with interatomic distances as large as 3.5–4 Å. These studies were conducted in vacuum, and attracted the interest of some computational theorists who attempted to explain this enigmatic stability using DFT [62, 63, 72]. In summary, the computational studies on the topic, which include AIMD [72], show that wires with interatomic distances beyond 2.6 Å dimerize. The converse is seen here in the presence of water where the originally zigzag chain extends to close to linearity as evident by Figure 3.26(b). Changes in the electronic structure in the presence of water might explain these observations.

To conclude this subsection on wire structure, Figure 3.27(a) shows the final vacuum optimized structure whereas Figure 3.27(b) shows a junction built using the average positions of the base, tip and wire atoms from the trajectory used for analysis. Differences can clearly be seen, including the elimination of an atom from the filament complex in the presence of water. Interatomic distances are around 2.8Å, close to 7% larger than their vacuum counterparts. To rationalize these observations as well as investigate the double layer further, electronic structure calculations are run.

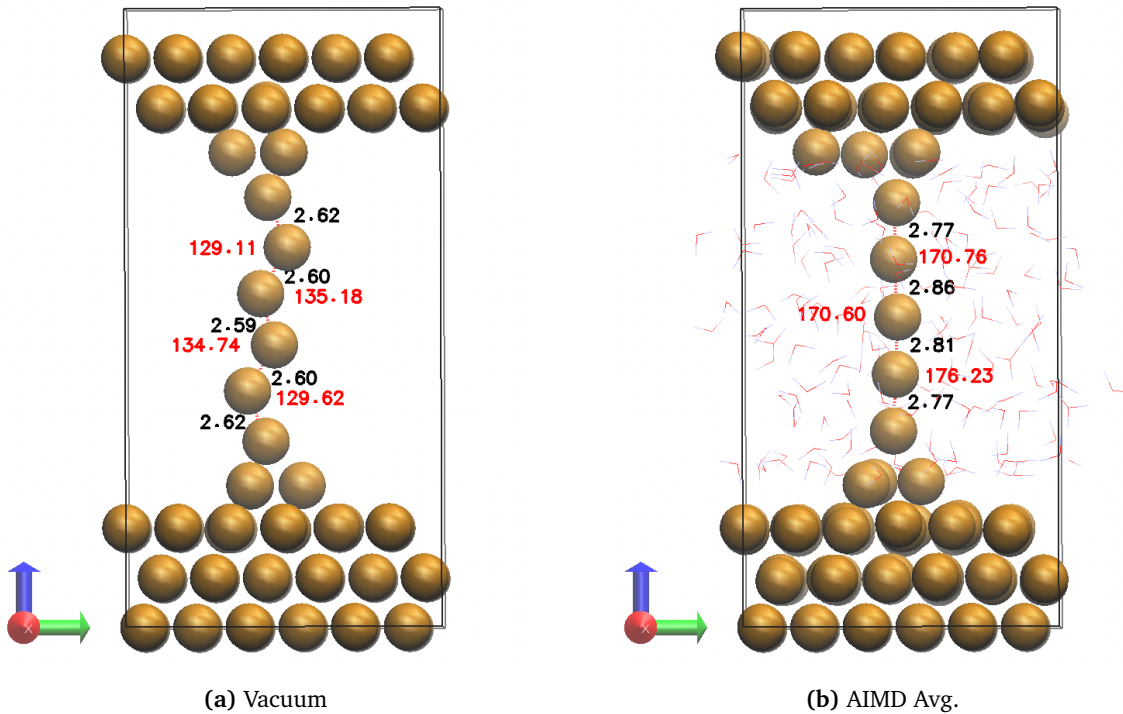


**Figure 3.27:** (a) Final structure obtained after cell optimization. (b) Average wire structure for last 2.425 picoseconds of AIMD run. Bond lengths and angles are labelled in black and red respectively.

### 3.5.4 Electronic Structure

Many central theorems in surface science have origins in the correlation between atomic and electronic structures at the interface which in turn govern properties such as charge transfer and mass transport that are of importance in engineering applications. For the purpose of electronic structures, charge density distributions and differences, PDOS and electrostatic potentials (ESP) will be investigated. Conclusions and insights can then be drawn by considering corresponding atomic and molecular structures in conjunction. For the purpose of electronic structure calculations, it is necessary to obtain averages from statistical samples, as was done in previous cases. Due to time constraints however, a single snapshot from 8.73 picoseconds of AIMD time is used. This snapshot resembles the average, artificial structure seen in Figure 3.27(b) and is part of the final few configurations close to equilibration. Therefore, subsequent analysis results should be considered at the very best as incomplete.

#### Electrostatic Potential

A start can be made by plotting the electrostatic potential (ESP) as a planar average in the z-direction. This direction is chosen in line with the junction shape. The ESP is a measure of charge distribution and provides useful information. At a given point, the ESP can be thought of as the work needed to bring a probe charge from infinity to that same point. For a positive charge, positive ESP values indicate repulsive forces are experienced at that point (relative to infinite separation) whereas the opposite is true for negative values. The ESP at a given point is the net effect of atomic nuclei and electrons such that in some systems, the least square method may be used to assign a set of charges to atoms/molecules that fit the ESP. It can be seen in Figure 3.28 that there are wells corresponding to electrode layers on either end of the junction. The ESP on either end are not equal, which should be the case when PBCs are applied. This might be caused by the inexactness of the interplanar spacing used for averaging the potential. In the region of the tips/wire (7–23 Å), the potential is irregular due to the presence of water. There are also differences in the average polarities with region containing the wire showing a positive potential. Moreover, there is a difference in potential of the 1st wire base (7Å) compared to the second (23Å) which contains an additional atom. Judging by the figure, there ought to be a greater pull of the wire in the direction of the upper electrode, which is observed in relative magnitudes of interatomic distances closer to the upper tip. As for the DL, no clear conclusions can be drawn from this plot.

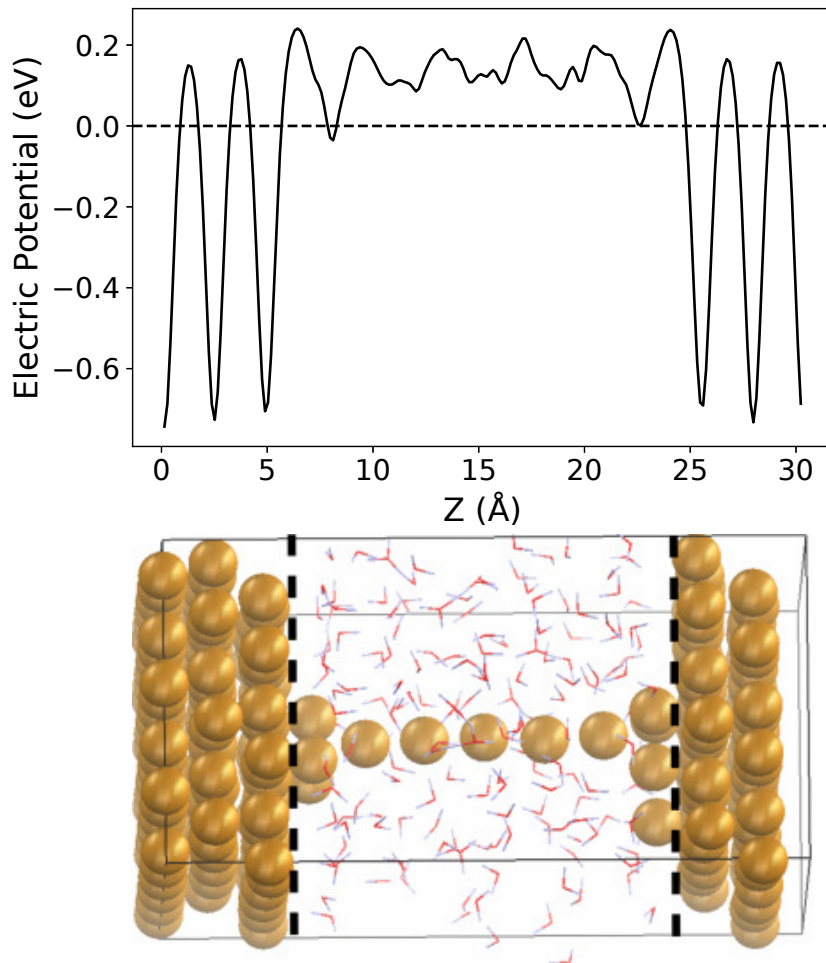


**Figure 3.28:** Planar average of the electrostatic potential in the z-direction using a single snapshot from the trajectory at 8.73 picoseconds

### Charge Density Difference

Metal/water interfaces involve charge redistribution related to atomic and molecular structures, specifically, water orientations close to exposed metal atoms. Charge redistribution is characteristic of chemical interactions, both covalent and coordinate, and can have important impacts on material properties including work functions of metals (reactivity) and changes in the potential of zero charge (PZC) [69]. It is useful to outline the different water-metal configurations and corresponding interactions. The water/metal configurations can be classified into three types: the O-down configuration ( $W_{M-O}$ ) which give rise to oxygen-density peaks closest to the surface (2.6 Å for Au(111)), the H-down configuration ( $W_{M-H}$ ) where hydrogen atoms are closer to the surface ( $\approx 2.1 \text{ \AA}$ ) and those with no preferred orientation ( $W_{free}$ ) [69]. Charge redistribution occurs from various contributions related to these water/metal configurations and can be observed in the form of charge density difference iso-surfaces or plots. To obtain these plots the total charge density corresponding to static energy runs on the metal atoms and water molecules separately, can be subtracted from the total charge density:

$$\Delta\rho(\mathbf{r}) = \rho_{M/W} - \rho_{M/V} - \rho_{W/V} \quad (3.8)$$

These operations are applied to the electron density cube file that can be printed as outputs in CP2K. Charge redistribution can be captured as regions of depletion and accumulation. The most prominent feature in Figure 3.29 is the striking yellow cloud surrounding the wire atoms. Several water molecules surrounding the wire have hydrogen atoms pointing towards the wire colored in cyan indicating electron depletion. The spaces between such H-down water molecules and the gold wire atoms show significant electron accumulation, clearly indicating covalent metal–hydrogen interactions. In the base atoms of the wire however, the water molecules are interacting with the metal differently. Most of the base atoms

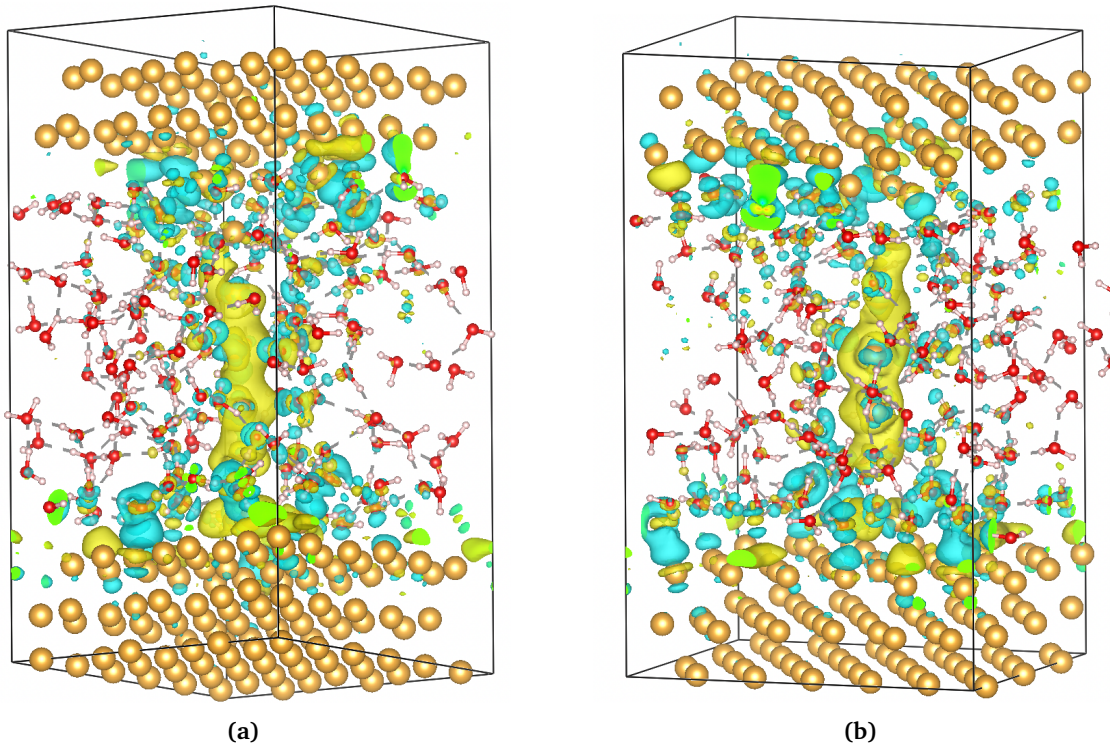


**Figure 3.29:** Charge density difference of the junction from two different angles (a) and (b) using a single snapshot from the trajectory at 8.73 picoseconds. Electron accumulation and depletion regions are colored in yellow and cyan respectively.

have water molecules of the O-down configuration directly interacting with them, with electron depletion regions in spaces between the metal–water pairs. As seen in the mass density profiles and other studies [69], density peaks for the O-down configuration on gold show a separation of around 2.6 Å, which is in the range of coordinate bonding. In such interactions, oxygen donates charge to the unoccupied orbitals of gold. The depletion region forming between  $W_{M-O}$  and the metal was suggested to be caused by Pauli repulsion according to Li et. al [69] between the electron spillover tail of the metal and  $W_{M-O}$ , which pushes the spilled electrons back to the metal skeleton. As for electrode surface layers, there is a mixture of  $W_{M-O}$  and  $W_{M-H}$  metal interactions on both surfaces and very few  $W_{free}$  metal interactions overall. In summary there appears to be a greater proclivity towards  $W_{M-H}$  metal interactions with decreasing gold coordination number. The continuous structuring seen outside the surface peaks in Figure 3.23 might be due to the significant shielding effects of the hydrogen–metal covalent bonds.

### Bader Charge Analysis

The 3D isosurface plot of Figure 3.29 provides an excellent picture of charge redistribution associated with the DL in the junction. It is beneficial to investigate the charges of the gold atoms, particularly the wire, in light of the different metal–water and gold–gold interactions. Bader charge analysis is commonly used for charge analysis in electrochemical systems [73]. Bader’s theory is based on the quantum theory of atoms in molecules (QTAIM), sometimes referred to as atoms in molecules (AIM). QTAIM uses the electronic density distribution function to express natural observables such as atoms and bonds [73]. In other words, the topology of the charge density is used to define bonds and structures. Here, Bader charge analysis will be used to obtain an approximation of the charges on the gold atoms in the system, including those in the wire. Cube file outputs from CP2K are processed using MATLAB to generate charge heat maps for the single snapshot at 8.73 picoseconds. The Bader charges on atoms in Figure 3.30 can be thought of as deviations from the charge density of an isolated gold atom such that negative charges indicate an excess in charge density and vice versa positive charges. The contrast in charge density across the junction is clear. The wire and tip atoms are significantly more negatively charged compared to the base and electrode atoms. This is understandable since the wire atoms are bonded to hydrogen. The middle three wire atoms are particularly negative, with charges of -0.2876, -0.2912 and -0.2825

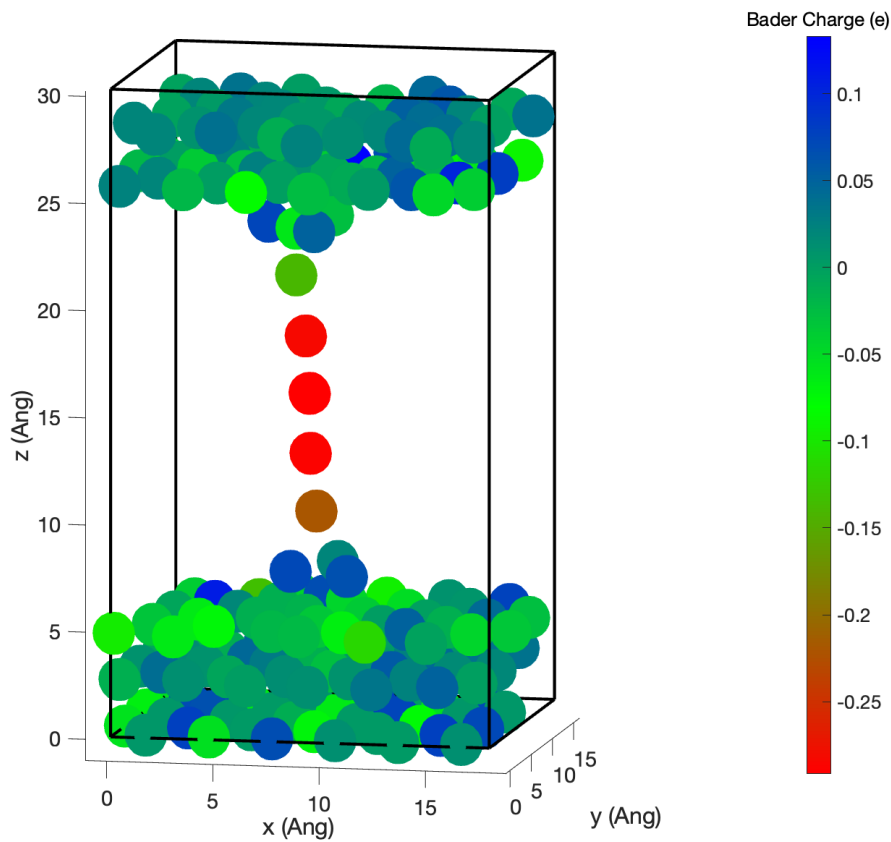


**Figure 3.30:** Bader charges of the junction gold atoms in the form of a charge–density map with the charge scale shown

(moving upwards). Although not easily apparent in Figure 3.29, more than one hydrogen atom appears to be bonded to a single wire atom. The base atoms on the other hand are mostly positive as they interact with  $W_{M-O}$  in a coordinate fashion. Charges on these atoms range from 0.07 to -0.05 (the negative atom on the upper base). On the electrode surfaces however, there is a mixture of positive and negative atoms (negative dominating) with charges influenced by the corresponding water interactions and delocalization of the charge density around gold atoms. Subsurface layers on the other hand are predominantly positive whereas the bulk (1st) layer is predominantly negative.

Figures 3.29 and 3.30 hold clues as to why the wire extends to such an extent in the presence of water. The electron accumulation around the wire atoms (and their negative charge) as well as the presence of positive base atoms, may induce repulsive forces between the middle wire atoms and attractive forces towards the electrodes that cause the wire to stretch in this manner. It is not unreasonable to believe that a similar effect may be responsible for the observation in the experimental study of Ohnishi et. al [71] if there are tiny amounts of moisture present in the system.

### Projected Density of States

Questions remain regarding the electronic structures of the wire atoms. With such large interatomic distances, the electronic structure of the wire might differ considerably from bulk gold, to the extent that conductivity might be altered. Moreover, the bonding between the gold atoms is also questionable. In attempts to address the aforementioned, the projected density of states (PDOS) was plotted. Firstly, the PDOS is plotted with the system broken down into three components: (1) the lower electrode, (2) base, tip and wire atoms and (3) the upper electrode. The system is intentionally broken down in a way that resembles that quantum point contact model used to study conductance [74]. Figure 3.31(a) shows a contrast in the available states in the electrodes and in the wire. There is a significant concentration of states closer to the Fermi level at around -2.4 eV in the case of the wire. There appears to be a

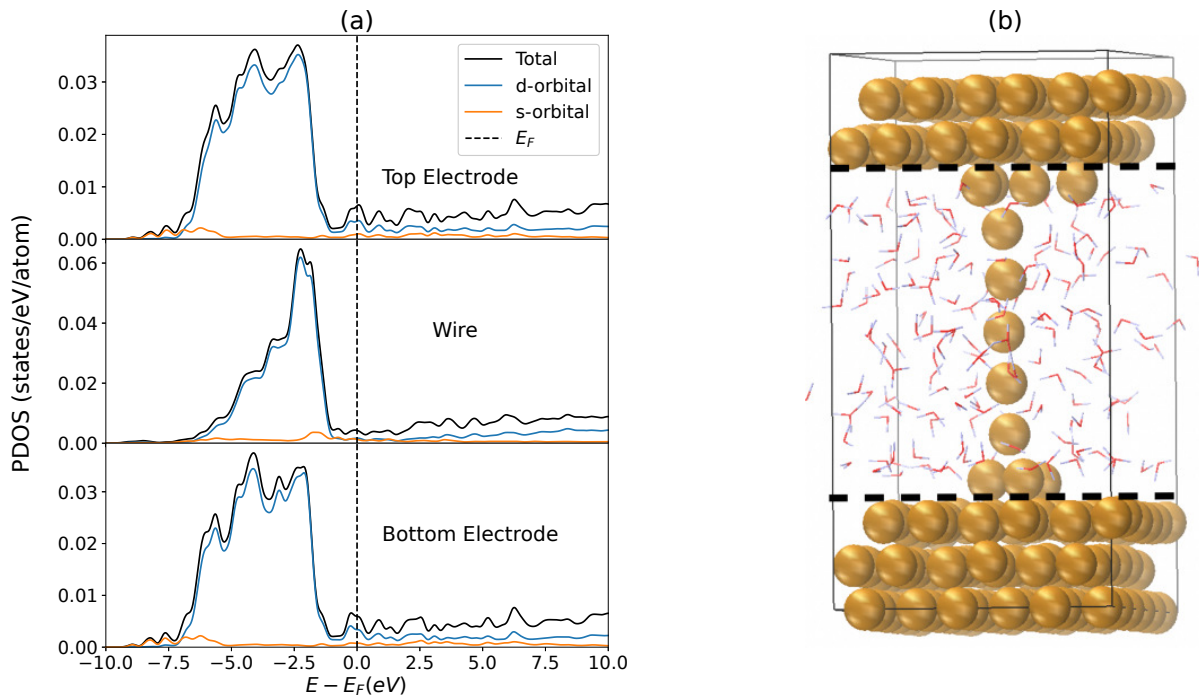


**Figure 3.31:** (a) PDOS of components of the junction using a single snapshot from the trajectory at 8.73 picoseconds. (b) Image of the junction with dotted lines separating the three components

greater number of available states overall, per atom, in the wire compared to the electrodes possibly due to interactions with water. The wire/base/tip complex maintains metallic and conductive properties as evident by the finite occupation at the Fermi level. However, the magnitude of the occupation at the Fermi level appears comparable or slightly less than that of the electrode atoms. The projected density of states of the three middle wire atoms are also plotted with the aim of investigating bonding between these atoms since overlapping peaks in PDOS diagrams indicate chemical bonds.

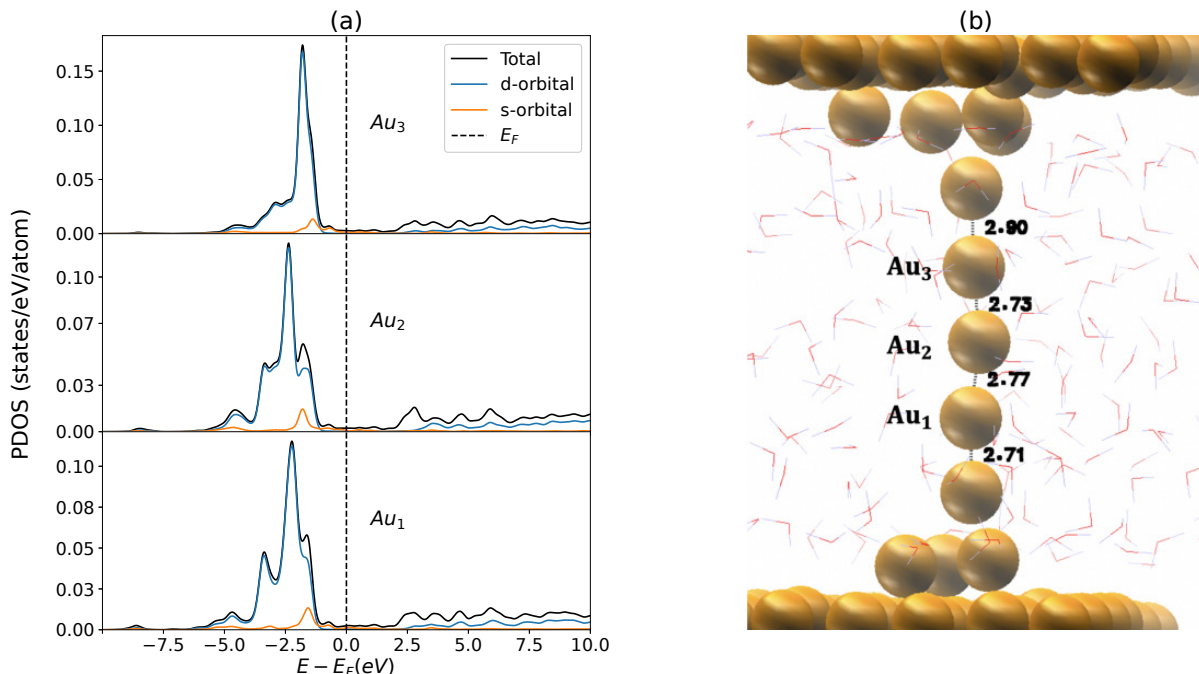


**Figure 3.32:** (a) PDOS plots of individual wire atoms (b) Image of the junction with corresponding wire atom labels and bond lengths in black

Figure 3.32(a) shows peaks around -2 eV for atoms  $Au_1$ ,  $Au_2$  and  $Au_3$  with significant s-orbital contributions. This was masked, or barely visible, in Figure 3.31. Such an increase in the s-orbital states is a result of bonding with hydrogen. The greatest s-orbital peak is seen for  $Au_2$  which has several hydrogen atoms bonded to it. As for bonds between gold atoms, another PDOS diagram is plotted to observe this more clearly.

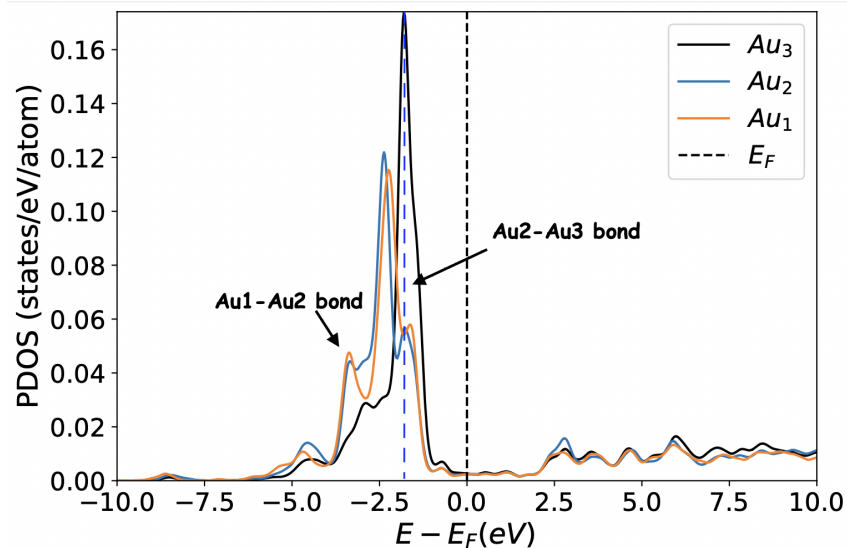


**Figure 3.33:** PDOS plots of individual wire atoms with bond overlaps labeled. The blue dashed line represents the position of overlap between peaks of  $Au_2$  and  $Au_3$  atoms

Overlaps in orbitals for the pair of atoms can now be observed clearly observed in Figure 3.33. The  $Au_1$ - $Au_2$  bond can be seen labelled on the plot. The  $Au_2$  –  $Au_3$  bond however is less clearly resolved. There are two possibilities which are labelled on the plot. In conclusion, there is evident bonding between the atom wires and the whole wire maintains conductivity. However, more calculations need to be run to get detailed information on conductivity and parameters such as surface reactivity as dynamic variables. Nonequilibrium's Green function (NEGF), which is implemented on CP2K, can be used to the conductance of the wire which may provide important insights that can be used to compare with experiments. This is left to future projects.

To summarize, within the scope of time available for this project, AIMD was run for a gold nanojunction in the present of explicit water molecules. Introductory work has been carried out here, with the little production run data available, in studying the structural evolution of the junction and the metal/water interface DL. Interesting observations were made which include a significant expansion of the wire in the presence of water. The mass density profiles hinted at the different water/metal interactions which were later confirmed by studying the charge density difference and Bader charges. Water was found to interact covalently with the wire and tip atoms through hydrogen, leading to relatively negative wire atoms, and coordinatively with the base atoms leading to positive charges on gold. These differences in bonding and charge redistribution were proposed as reasons for the expansion of the wire. The PDOS of the wire atoms confirmed bonding between them. However, the exact origin of the stability of the wire at such stretched lengths is not clear and not enough information is available to make comments on conductance through the wire and its transformation in the presence of water.

# Future Work

There are many pathways to improve and build on this work. Beginning with the latter, the most obvious step that could be taken is run at least 40 picoseconds of AIMD to obtain sufficient data for statistical average and to give sufficient time for micro-processes to unfold. Analysis can then be more expansive and meaningful. Analysis of AIMD results can also be extended to cover more electronic structure calculations, including PDOS for the different layers. The simplifications made here mean there are manifold steps/details that could be added the most central being the application of a bias. Ions could also be included (modelling an electrolyte) before adding a molecule between the two electrodes/wire. In more detail, adsorbates can be added to the 'dry' and optimized junction in the form of water bi-layers (H, OH) with different configurations (H-up, H-down). The coverage could then be measured as a function of the applied potential following the approach of Nørskov. Next, water could be added to the system and transformations in the water layer and the wire can be investigated under the influence of a bias. Ions can also be added, such as water autoionization productions hydroxyl and hydronium, and the ion unbalance method could be applied to control the potential posteriori. A significantly fruitful undertaking would be to also apply non-equilibrium green function (NEGF), which is implemented on CP2K, to study conductance through the junction. This could be repeated for the 'dry' junction, when adsorbates are added and for different snapshots from the AIMD trajectory corresponding to different structures. Using NEGF is particularly fruitful as it opens up the possibility of comparing with a wealth of experimental data available in the literature. In addition to the aforementioned tests on the nanowire-based system, these could be applied to setups with a molecule bridging the two wires/electrodes.

The work done here on silver could also be built upon. Silver is a common material for active electrodes in electrochemical metallization memories (ECM). The phenomenon of electrochemical metallization is very interesting and ECM devices are highly attractive devices for next-generation computers such as neuromorphic computers. Electrochemical metallization involves the formation/rupture of a metallic filament between an active electrode (e.g. silver) and an inert electrode (e.g. Pt) and has been noted to occur both using solid electrolytes and liquids (water). An interesting line of investigation resembling the AIMD work done undertaken here would be to set up a chemically symmetric silver nanojunction and investigate the dynamics of wire rupture/formation in the presence of bias and electrolytic, water environment. Such work could serve to understand some of the origins of variability, irregularity and stochasticity during device operation which act as the major barrier towards device commercialization.

# Conclusion

A solvated gold nanojunction was successfully setup and investigated using AIMD. The setup first included modelling bulk gold and gold electrodes using DFT. Silver was modelled in addition as a metal of importance in nanoelectronics. For the bulk metals similar values for the simulation parameters of silver and gold were required to minimize total energy errors. These are summarized as  $14x14x14$  k-points,  $cutoff = 300Ry$ ,  $relicutoff = 450Ry$  and the TZVP MOLOPT basis set. The lattice parameters and electronic structures agreed closely with other DFT-GGA simulations. In the case of the latter, the underestimation in the band gap common to DFT was apparent. When modelling the electrodes using slab geometries, more stringent requirements for simulation parameters were found with  $12x12x1$  k-points required for  $2x2xN$  electrodes as well as a  $cutoff = 500Ry$  based on the surface energy and work functions of the slabs. The slab surface energies were better converged than the work function when the number of layers was increased to 16, suggesting that a few more additional layers are needed for full convergence. Tests with the slab geometry revealed that 5 layer slabs offer a good compromise between computational costs and accuracy with values of  $0.0434 \pm 0.0015\text{eV}$  and  $5.21 \pm 0.053\text{eV}$  for surface energy and work function respectively. The suitability of the 5-layer slab was further established by plotting the PDOS of its middle layer and comparing to bulk. The setup of the 'dry' junction was topped off with a cell optimization which proved efficient as a method to obtain a reasonable and metastable structure, in the form of a zigzag shape for the wire.

Detailed hand-calculations also proved sufficient in evaluating the 'correct' number of water molecules to be added to the junction to meet the room-temperature density of water. Ideally classical MD following the NPT ensemble should be used. However, this proved unfeasible using the supercell determined in this study since water's incompressibility leads to variations in pressure in the metal that cause an immediate destruction of the wire. This is hard to avoid using classical MD. It was sufficient to run using the NVT ensemble where a water structure in agreement with other TIP3P simulations was obtained, with  $30\text{ns}$  of MD time achieved quickly. Immediate differences were when AIMD was run, on a structural and electronic level. For the former, it can be concluded that the wire prefers a more linear shape and is 'flattened' in the presence of water. Throughout the duration of the AIMD (roughly 8.9 picoseconds), the wire showed no tendency towards rupturing, indicating the possibility of stable single atom thick wires suspended between electrodes in water. However, no further statements can be made in this regard with the available data.

There is a good agreement in the mass density and RDF results here with other AIMD studies related to metal/water interfaces and gold in particular despite the minimal statistics. Interesting insights can be drawn from the subsequent electronic structure analysis (which should be weighed considering that only a single snapshot was used). Water prefers a H-down orientation near wire atoms which leads to covalent Au-H bonds that alter the charge and electronic structure of the wire relative to the base atoms, which water interacts with through the O-down orientation forming coordinate bonds, as well as bulk gold. The charge alteration/profile can be clearly captured by applying Bader charge analysis. A tentative explanation of the expansion of the wire in the presence of water is that electrostatic interactions arising from the charge around the wire atoms as well polarity differences along the junction, might cause the stretching of the bond. Finally, it can be concluded from PDOS diagrams that the wire atoms are chemically bonded and retain metallic/conductive properties.

# Appendix

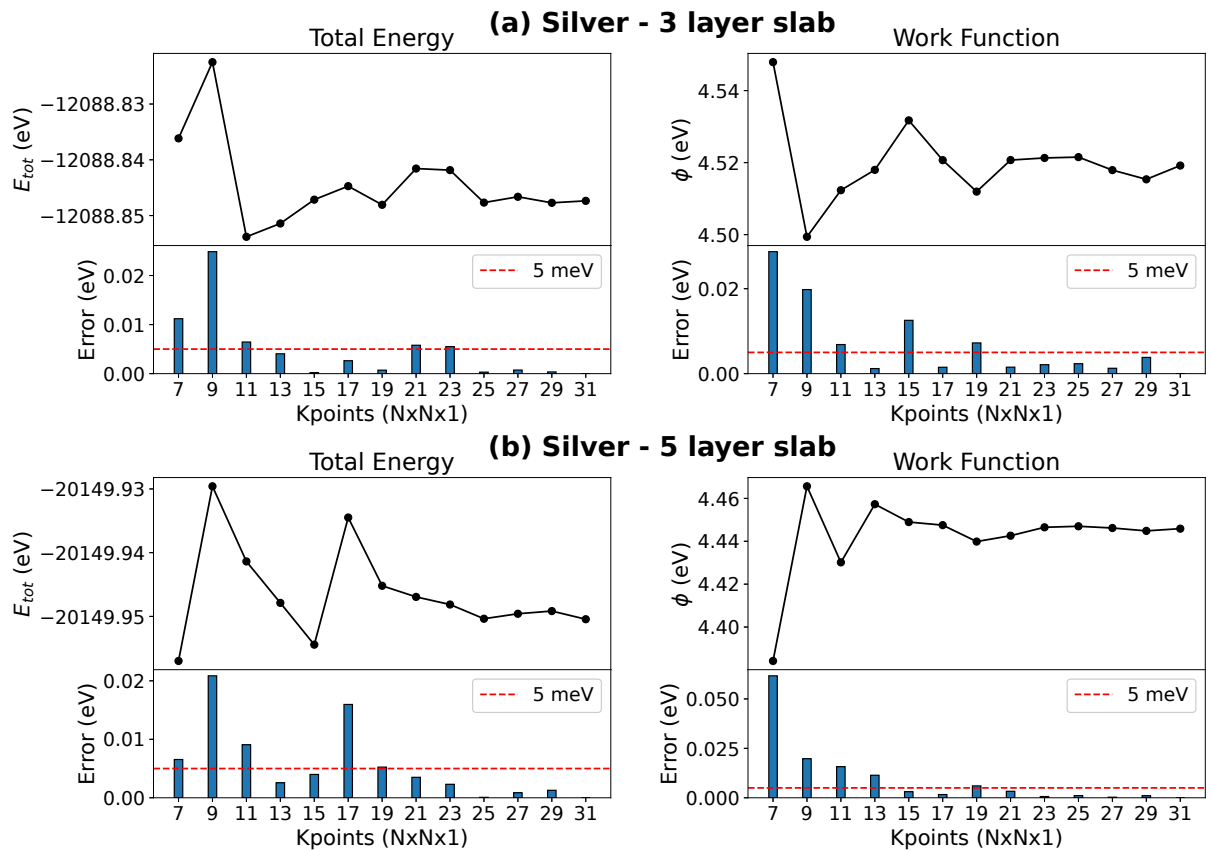


Figure A.1: K-points convergence tests on (a) 2x2x3 and (b) 2x2x5 silver slabs

# Bibliography

1. Koper, M. T., Weber, A. Z., Chan, K. & Cheng, J. *Introduction: Computational Electrochemistry* 2022.
2. Sundararaman, R., Vigil-Fowler, D. & Schwarz, K. Improving the Accuracy of Atomistic Simulations of the Electrochemical Interface. *Chemical Reviews* (2022).
3. Groß, A. & Sakong, S. Ab Initio Simulations of Water/Metal Interfaces. *Chemical Reviews* (2022).
4. Payne, R. The electrical double layer: Problems and recent progress. *Journal of Electroanalytical Chemistry and Interfacial Electrochemistry* **41**, 277–309 (1973).
5. Sakong, S. & Groß, A. The electric double layer at metal-water interfaces revisited based on a charge polarization scheme. *The Journal of chemical physics* **149**, 084705 (2018).
6. Khatib, R., Kumar, A., Sanvito, S., Sulpizi, M. & Cucinotta, C. S. The nanoscale structure of the Pt-water double layer under bias revealed. *Electrochimica Acta* **391**, 138875 (2021).
7. Santos, E. & Schmickler, W. Models of Electron Transfer at Different Electrode Materials. *Chemical Reviews* (2022).
8. Tang, Z. *et al.* Solvent-molecule interaction induced gating of charge transport through single-molecule junctions. *Science Bulletin* **65**, 944–950 (2020).
9. Mathew, P. T. & Fang, F. Advances in molecular electronics: a brief review. *Engineering* **4**, 760–771 (2018).
10. Wang, L., Wang, L., Zhang, L. & Xiang, D. Advance of mechanically controllable break junction for molecular electronics. *Molecular-Scale Electronics*, 45–86 (2019).
11. Vuillaume, D. Molecular nanoelectronics. *Proceedings of the IEEE* **98**, 2111–2123 (2010).
12. Vladyka, A. *Detailed analysis of single molecular junctions for novel computing architectures* PhD thesis (University\_of\_Basel, 2017).
13. Pacchioni, G. Improving memristors' reliability. *Nature Reviews Materials*, 1–1 (2022).
14. Chen, Z.-B. *et al.* Gold atomic contact: Electron conduction in the presence of interfacial charge transfer. *Electrochemistry communications* **47**, 41–44 (2014).
15. Nichols, R. J. & Higgins, S. J. Single molecule nanoelectrochemistry in electrical junctions. *Accounts of chemical research* **49**, 2640–2648 (2016).
16. Li, Y., Kaneko, S., Fujii, S., Nishino, T. & Kiguchi, M. Atomic structure of water/Au, Ag, Cu and Pt atomic junctions. *Physical Chemistry Chemical Physics* **19**, 4673–4677 (2017).
17. Leroux, Y. R., Fave, C., Zigah, D., Trippe-Allard, G. & Lacroix, J. C. Atomic contacts via electrochemistry in water/cyclodextrin media: a step toward protected atomic contacts. *Journal of the American Chemical Society* **130**, 13465–13470 (2008).
18. Senftle, T. P. *et al.* The ReaxFF reactive force-field: development, applications and future directions. *npj Computational Materials* **2**, 1–14 (2016).
19. Valov, I., Waser, R., Jameson, J. R. & Kozicki, M. N. Electrochemical metallization memories—fundamentals, applications, prospects. *Nanotechnology* **22**, 254003 (2011).
20. Sholl, D. S. & Steckel, J. A. *Density functional theory: a practical introduction* (John Wiley & Sons, 2011).
21. Essén, H. The physics of the born–oppenheimer approximation. *International Journal of Quantum Chemistry* **12**, 721–735 (1977).
22. Flick, J., Rivera, N. & Narang, P. Strong light-matter coupling in quantum chemistry and quantum photonics. *Nanophotonics* **7**, 1479–1501 (2018).
23. Hohenberg, P. & Kohn, W. Inhomogeneous electron gas. *Physical review* **136**, B864 (1964).
24. Sham, L. J. & Kohn, W. One-particle properties of an inhomogeneous interacting electron gas. *Physical Review* **145**, 561 (1966).
25. Ernzerhof, M. & Scuseria, G. E. Assessment of the Perdew–Burke–Ernzerhof exchange-correlation functional. *The Journal of chemical physics* **110**, 5029–5036 (1999).
26. Kadaoluwa Pathirannahalage, S. P. *et al.* Systematic comparison of the structural and dynamic properties of commonly used water models for molecular dynamics simulations. *Journal of Chemical Information and Modeling* **61**, 4521–4536 (2021).

27. Kratzer, P. & Neugebauer, J. The basics of electronic structure theory for periodic systems. *Frontiers in chemistry* **7**, 106 (2019).
28. Lin, L., Lu, J. & Ying, L. Numerical methods for Kohn–Sham density functional theory. *Acta Numerica* **28**, 405–539 (2019).
29. Chadi, D. J. & Cohen, M. L. Special points in the Brillouin zone. *Physical Review B* **8**, 5747 (1973).
30. Monkhorst, H. J. & Pack, J. D. Special points for Brillouin-zone integrations. *Physical review B* **13**, 5188 (1976).
31. Kühne, T. D. *et al.* CP2K: An electronic structure and molecular dynamics software package-Quickstep: Efficient and accurate electronic structure calculations. *The Journal of Chemical Physics* **152**, 194103 (2020).
32. Tuckerman, M. E. & Martyna, G. J. *Understanding modern molecular dynamics: Techniques and applications* 2000.
33. Braun, E., Moosavi, S. M. & Smit, B. Anomalous effects of velocity rescaling algorithms: the flying ice cube effect revisited. *Journal of chemical theory and computation* **14**, 5262–5272 (2018).
34. Praprotnik, M. & Janežič, D. Molecular dynamics integration and molecular vibrational theory. III. The infrared spectrum of water. *The Journal of chemical physics* **122**, 174103 (2005).
35. Berg, A., Peter, C. & Johnston, K. Evaluation and optimization of interface force fields for water on gold surfaces. *Journal of Chemical Theory and Computation* **13**, 5610–5623 (2017).
36. Grochola, G., Russo, S. P. & Snook, I. K. On fitting a gold embedded atom method potential using the force matching method. *The Journal of chemical physics* **123**, 204719 (2005).
37. Ryu, S., Weinberger, C. R., Baskes, M. I. & Cai, W. Improved modified embedded-atom method potentials for gold and silicon. *Modelling and Simulation in Materials Science and Engineering* **17**, 075008 (2009).
38. CP2K. *How to run IC-QM/MM simulations for interface systems* <https://www.cp2k.org/howto:ic-qmmm>, Last accessed on 2022-08-17. 2021.
39. Hutter, J. Car–Parrinello molecular dynamics. *Wiley Interdisciplinary Reviews: Computational Molecular Science* **2**, 604–612 (2012).
40. Tyuterev, V. & Vast, N. Murnaghan’s equation of state for the electronic ground state energy. *Computational materials science* **38**, 350–353 (2006).
41. Yoo, S.-H., Lee, J.-H., Jung, Y.-K. & Soon, A. Exploring stereographic surface energy maps of cubic metals via an effective pair-potential approach. *Physical Review B* **93**, 035434 (2016).
42. Fiorentini, V. & Methfessel, M. Extracting convergent surface energies from slab calculations. *Journal of Physics: Condensed Matter* **8**, 6525 (1996).
43. Lang, N. & Kohn, W. Theory of metal surfaces: work function. *Physical Review B* **3**, 1215 (1971).
44. Maeland, A. & Flanagan, T. B. Lattice spacings of gold–palladium alloys. *Canadian journal of physics* **42**, 2364–2366 (1964).
45. Shi, H., Asahi, R. & Stampfl, C. Properties of the gold oxides Au<sub>2</sub>O<sub>3</sub> and Au<sub>2</sub>O: First-principles investigation. *Physical Review B* **75**, 205125 (2007).
46. Kong, G.-X., Ma, X.-J., Liu, Q.-J., Li, Y. & Liu, Z.-T. Structural stability, elastic and thermodynamic properties of Au–Cu alloys from first-principles calculations. *Physica B: Condensed Matter* **533**, 58–62 (2018).
47. Yu, B. D. & Scheffler, M. Physical origin of exchange diffusion on fcc (100) metal surfaces. *Physical Review B* **56**, R15569 (1997).
48. Janthon, P. *et al.* Bulk properties of transition metals: a challenge for the design of universal density functionals. *Journal of chemical theory and computation* **10**, 3832–3839 (2014).
49. Singh-Miller, N. E. & Marzari, N. Surface energies, work functions, and surface relaxations of low-index metallic surfaces from first principles. *Physical Review B* **80**, 235407 (2009).
50. Klimeš, J., Bowler, D. R. & Michaelides, A. Van der Waals density functionals applied to solids. *Physical Review B* **83**, 195131 (2011).
51. Hinuma, Y., Pizzi, G., Kumagai, Y., Oba, F. & Tanaka, I. Band structure diagram paths based on crystallography. *Computational Materials Science* **128**, 140–184 (2017).

52. Aflow Advanced Search <http://aflow.org/search/>, Last accessed on 2022-08-17. 2022.
53. Christensen, N. E. & Seraphin, B. Relativistic band calculation and the optical properties of gold. *Physical Review B* **4**, 3321 (1971).
54. Ramchandani, M. Energy band structure of gold. *Journal of Physics C: Solid State Physics* **3**, S1 (1970).
55. Rangel, T. *et al.* Band structure of gold from many-body perturbation theory. *Physical Review B* **86**, 125125 (2012).
56. Hegde, R. S. & Khatua, S. in *Nanoelectronics* 289–315 (Elsevier, 2019).
57. Perdew, J. P. Density functional theory and the band gap problem. *International Journal of Quantum Chemistry* **28**, 497–523 (1985).
58. Liu, Z.-P., Hu, P. & Alavi, A. Catalytic role of gold in gold-based catalysts: A density functional theory study on the CO oxidation on gold. *Journal of the American Chemical Society* **124**, 14770–14779 (2002).
59. Christensen, N. E. The band structure of silver and optical interband transitions. *physica status solidi (b)* **54**, 551–563 (1972).
60. Patra, A., Bates, J. E., Sun, J. & Perdew, J. P. Properties of real metallic surfaces: Effects of density functional semilocality and van der Waals nonlocality. *Proceedings of the National Academy of Sciences* **114**, E9188–E9196 (2017).
61. Derry, G. N., Kern, M. E. & Worth, E. H. Recommended values of clean metal surface work functions. *Journal of Vacuum Science & Technology A: Vacuum, Surfaces, and Films* **33**, 060801 (2015).
62. Sánchez-Portal, D. *et al.* Stiff monatomic gold wires with a spinning zigzag geometry. *Physical review letters* **83**, 3884 (1999).
63. De Maria, L. & Springborg, M. Electronic structure and dimerization of a single monatomic gold wire. *Chemical Physics Letters* **323**, 293–299 (2000).
64. Weisstein, E. W. Spherical triangle. <https://mathworld.wolfram.com/> (2004).
65. Martínez, L., Andrade, R., Birgin, E. G. & Martínez, J. M. PACKMOL: A package for building initial configurations for molecular dynamics simulations. *Journal of computational chemistry* **30**, 2157–2164 (2009).
66. Wade, A. D., Wang, L.-P. & Huggins, D. J. Assimilating radial distribution functions to build water models with improved structural properties. *Journal of chemical information and modeling* **58**, 1766–1778 (2018).
67. Camisasca, G., Pathak, H., Wikfeldt, K. T. & Pettersson, L. G. Radial distribution functions of water: Models vs experiments. *The Journal of chemical physics* **151**, 044502 (2019).
68. Mark, P. & Nilsson, L. Structure and dynamics of the TIP3P, SPC, and SPC/E water models at 298 K. *The Journal of Physical Chemistry A* **105**, 9954–9960 (2001).
69. Li, P., Huang, J., Hu, Y. & Chen, S. Establishment of the potential of zero charge of metals in aqueous solutions: Different faces of water revealed by ab initio molecular dynamics simulations. *The Journal of Physical Chemistry C* **125**, 3972–3979 (2021).
70. Pamato, M. G., Wood, I. G., Dobson, D. P., Hunt, S. A. & Vočadlo, L. The thermal expansion of gold: point defect concentrations and pre-melting in a face-centred cubic metal. *Journal of applied crystallography* **51**, 470–480 (2018).
71. Ohnishi, H., Kondo, Y. & Takayanagi, K. Quantized conductance through individual rows of suspended gold atoms. *Nature* **395**, 780–783 (1998).
72. Torres, J. *et al.* The puzzling stability of monatomic gold wires. *Surface science* **426**, L441–L446 (1999).
73. Tang, W., Chill, S. & Henkelman, G. *Bader charge analysis* 1970.
74. Lian, X. *et al.* Multi-scale quantum point contact model for filamentary conduction in resistive random access memories devices. *Journal of Applied Physics* **115**, 244507 (2014).